Tectonics

RESEARCH ARTICLE
10.1029/2019TC005951

Special Section:
Tethyan dynamics: from rifting to collision

Reconciling Orogenic Drivers for the Evolution of the Bangong-Nujiang Tethys During Middle-Late Jurassic

Shi-Min Li[1], Qing Wang[1], Di-Cheng Zhu[1], Peter A. Cawood[2], Robert J. Stern[3], Roberto Weinberg[2], Zhidan Zhao[1], and Xuan-Xue Mo[1]

[1]State Key Laboratory of Geological Processes and Mineral Resources, and School of Earth Science and Resources, China University of Geosciences, Beijing, China, [2]School of Earth, Atmosphere and Environment, Monash University, Melbourne, Victoria, Australia, [3]Geosciences Department, University of Texas at Dallas, Richardson, TX, USA

Abstract Identifying arc-trench systems along with spatial and temporal variations in their record of tectono-magmatic events is crucial for determining the orogenic divers and evolution of orogenic systems. New geochronological and geochemical data of Jurassic igneous rocks, as well as detrital zircon data from contemporaneous sedimentary units, within the eastern Bangong-Nujiang suture in central Tibet indicate the existence of an approximately 1,200-km Middle-Late Jurassic magmatic arc system. This arc system can be divided into two distinct along-strike segments, which are characterized by magmatic activity extending from 166 to 160 Ma in the east and 170–148 Ma in the west, followed by magmatic gaps at 160–120 and 148–125 Ma, respectively. An accretionary prism, magmatic arc, and retro-arc sedimentary units are identified from south to north in the eastern segment. The 166–160 Ma arc includes high-K calc-alkaline granitoids, and high-Mg andesites, dacites, and rhyolites, which collectively can be interpreted to originate from partial melting of ancient lower crust and mélange diapirs above a north dipping subduction zone. Our analysis reveals the existence of an overall compressional arc-trench system along strike, which overlaps with a phase of 170–160 Ma ophiolite generation and a rock association of 160–148 Ma slab-derived adakites and oceanic island basalt-type rocks, and is followed by an overall magmatic gap during 148–125 Ma with subsequent 125–105 Ma extensive magmatism. We infer that these records may reflect sequential tectonic events, including subparallel ridge-trench collision (170–160 Ma), slab window formation (160–148 Ma), subsequent subduction termination (148–125 Ma), and final Lhasa-Qiangtang amalgamation (125–105 Ma).

Key Points:
- An ~1,200-km-long Middle-Late Jurassic magmatic arc flanked by coeval sedimentary units
- An overall compressional convergent margin overlapping with ophiolite generation and slab window magmatism, and followed by a magmatic gap
- Sequential events including subparallel ridge-trench collision, slab window formation, subduction termination, and Lhasa-Qiangtang amalgamation

Supporting Information:
- Supporting Information S1
- Tables S1–S7

Correspondence to:
D.-C. Zhu,
dchengzhu@163.com

Citation:
Li, S.-M., Wang, Q., Zhu, D.-C., Cawood, P. A., Stern, R. J., Weinberg, R., et al. (2020). Reconciling orogenic drivers for the evolution of the Bangong-Nujiang Tethys during Middle-Late Jurassic. *Tectonics*, *39*, e2019TC005951. https://doi.org/10.1029/2019TC005951

Received 28 OCT 2019
Accepted 17 JAN 2020
Accepted article online 22 JAN 2020

Resubmitted to Tectonics (January 14, 2020)

1. Introduction

Collisional orogenic belts involve an initial accretionary episode of oceanic slab subduction and subsequent continental collision (Cawood et al., 2009; Dewey & Spall, 1975; Murphy & Nance, 1991; Zhu et al., 2019). The magmatic systems that develop on the upper plate during subduction and initial collision record the processes of convergence and orogenesis (Cawood et al., 2009; Stern, 2002; Zhu et al., 2019). Potential geodynamic divers for orogenesis during accretionary and collisional stages (Figure 1) include subduction initiation (Stern & Gerya, 2018), buoyant lithosphere subduction (e.g., oceanic plateau; Martinod et al., 2010), mid-ocean ridge subduction (Georgieva et al., 2019), and continental lithosphere collision (Kapp & DeCelles, 2019; Zhu et al., 2015, 2019). Determining the divers of orogenesis is crucial for unraveling orogenic evolution, but is often difficult to resolve because of incomplete preservation of the geological record and contrasting interpretations of the record that is preserved. For example, both ridge subduction (Gorring & Kay, 2001) and slab break-off during continental collision (Zhu et al., 2015) can generate slab window magmatism, or estimates for the timing of continental collision and magmatic response, even for well-studied modern orogens such as the Himalaya, can vary significantly (e.g., Hu et al., 2016; Zhu et al., 2019). Although orogens have a long record of formation and stabilization, the dynamic divers of orogenesis, especially those associated with accretionary orogens, are generally shorted-lived and transient (e.g., subduction initiation; Reagan et al., 2019) or diachronous (e.g., oblique ridge subduction; Breitsprecher & Thorkelson, 2009). The effects of these divers could be local (e.g., oceanic plateau; Martinod et al., 2010) or regional (e.g., continental collision; Zhu et al., 2019; Kapp &

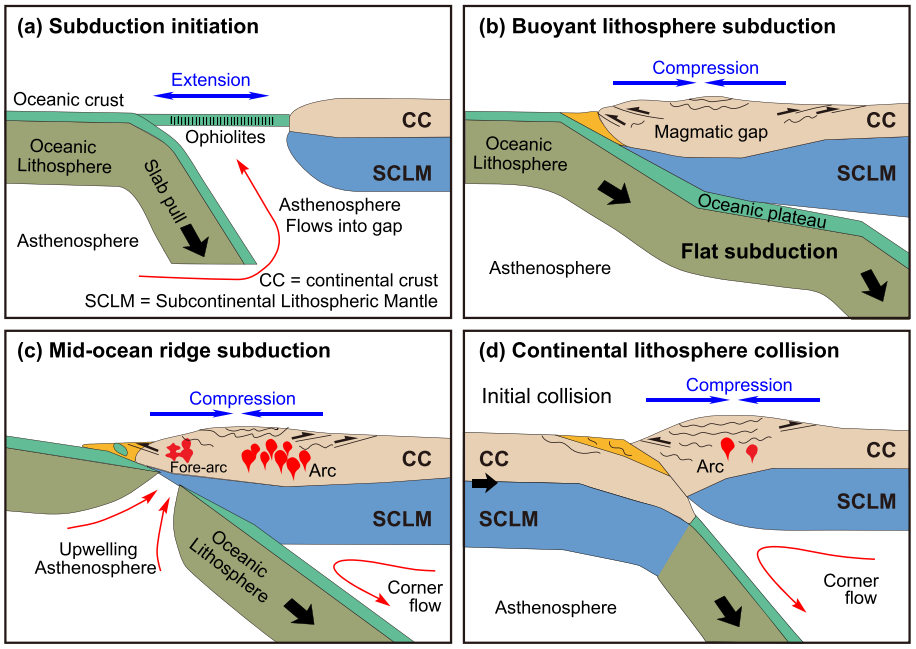

Figure 1. Cartoon showing the potential geodynamic divers for orogenesis during accretionary and collisional stages, including (a) subduction initiation, (b) buoyant lithosphere subduction (e.g., oceanic plateau), (c) mid-ocean ridge subduction, and (d) continental lithosphere collision.

DeCelles, 2019) in scale and can take place within a regime of ongoing subduction or at the termination of subduction (Cawood et al., 2009). Important clues in constraining the divers of orogenesis can be provided by recognition of long-term arc-trench systems and understanding the time-space distribution of tectono-magmatic events (Cawood et al., 2009).

The E-W trending Bangong-Nujiang suture (BNS; Figures 2a and 2b) in central Tibet separates the Lhasa and Qiangtang Terranes (Kapp & DeCelles, 2019; Zhu et al., 2016). Assembly of the terranes is related to an overall environment of ocean closure and continental collision, but a range of drivers and kinematic scenarios have been invoked for northward subduction based on the rock archive within the BNS and Qiangtang Terrane, including subduction initiation inferred from ophiolites (188–165 Ma; Figure 1a; Tang, Zhai, Hu, Xiao, et al., 2018) and high-Mg andesites (approximately 163 Ma; Y.C. Zeng, Chen, et al., 2016), Lhasa-Qiangtang collision on the basis of angular unconformities (approximately 166 Ma; Figure 1 d; Ma et al., 2017; Li, Guilmette, et al., 2017; Sun et al., 2018), and ridge subduction from a rock association of adakites and oceanic island basalt (OIB)-type rocks (160–148 Ma; Figure 1c; S.M. Li, Zhu, et al., 2016; Y.L. Li, He, et al., 2016). Evaluating and resolving this diversity of proposed scenarios requires reconstruction of the arc-trench system associated with terrane assembly, and integrating the comprehensive suite of geological information that has accumulated in recent years with our ongoing studies.

This paper provides new zircon U-Pb ages and geochemical data of igneous rocks and detrital zircon ages of sandstones in the eastern BNS. Our analysis reveals the existence of an overall compressional arc-trench system divisible from south to north into an accretionary prism, magmatic arc, and retro-arc sedimentary units, which can be traced over 1,200 km along strike. Magmatic activity within the arc ranges from 166 to 160 and 170–148 Ma in the eastern and western segments, respectively, overlaps with a phase of ophiolite generation (170–160 Ma) and a rock association of adakites and OIB-type rocks (160–148 Ma), and is succeeded by a prolonged magmatic gap (overall 148–125 Ma) and subsequent extensive magmatism (125–105 Ma). We propose that this sequence of tectonic events can be integrated into an evolving geodynamic setting involving trench-parallel ridge collision (170–160 Ma), slab window formation (160–148 Ma), subsequent subduction termination (148–125 Ma), and final Lhasa-Qiangtang amalgamation (125–105 Ma). Our study signifies the importance of a comprehensive integration of existing geological data to reconstruct the entire history of ancient orogenic belts.

10.1029/2019TC005951

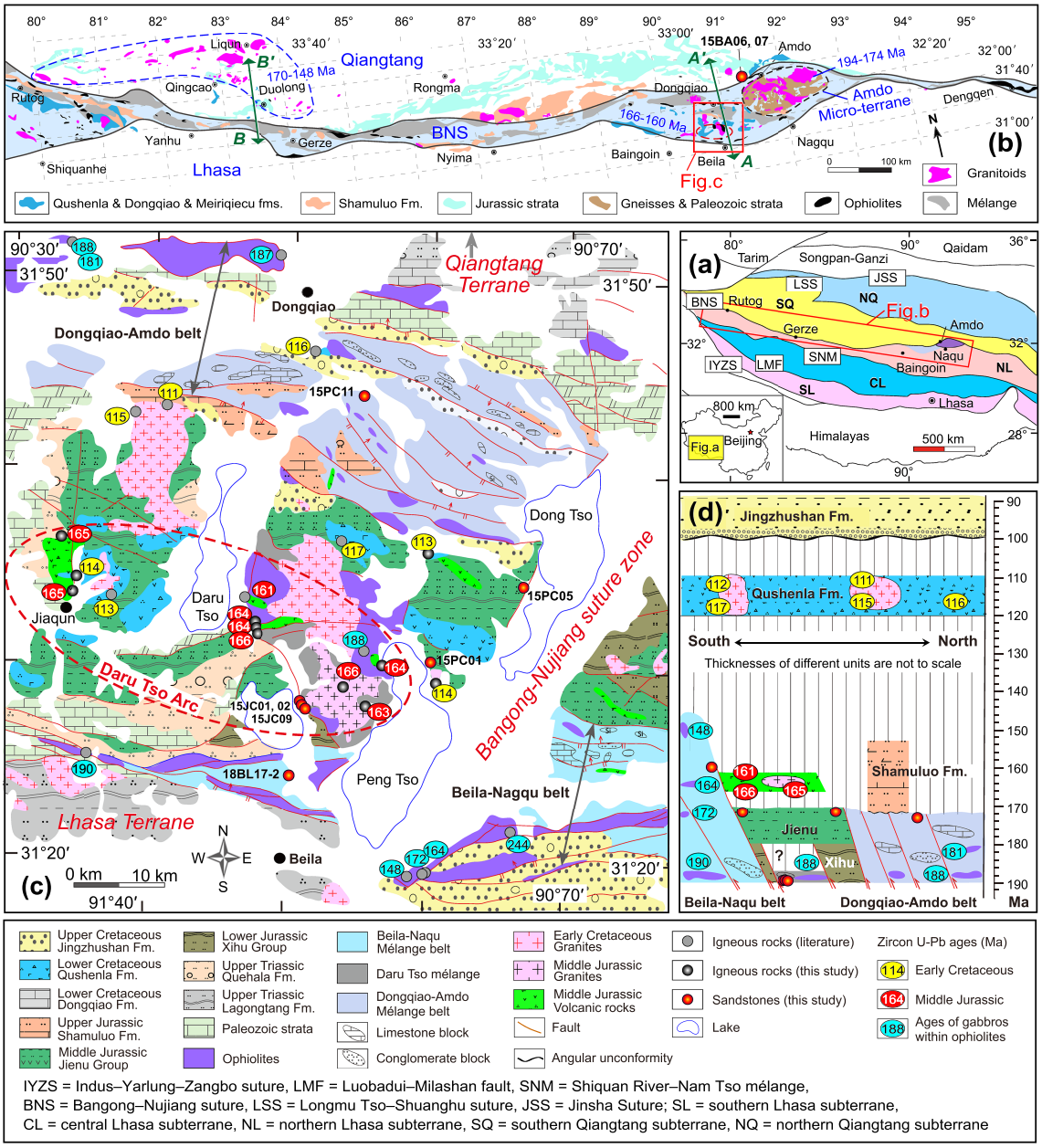

Figure 2. (a) Simplified tectonic framework of Tibetan Plateau (Zhu et al., 2013). (b) Simplified geological map of the BNS and SQ (modified from Zhu et al., 2016). The A-A′ and B-B′ are the locations of simplified cross sections in Figure 8. (c and d) Geological map and cross section of the Beila-Dongqiao region within the BNS (modified after the Regional Geological Survey of 1: 250,000 Baingoin Sheet, 2006). Ages of igneous rocks are from X. Li et al. (2015), Y.C. Zeng, Chen, et al. (2016), Hu et al. (2017), and Wu et al. (2018). Ages of ophiolitic mafic rocks are from Zhong, Liu, et al. (2017), Tang, Zhai, Hu, Wang, et al. (2018), and X.C. Wang et al. (2018).

2. Geological Background

Central Tibet contains from north to south, two E-W trending terranes (Figure 2a): the Qiangtang and Lhasa Terranes, separated by the BNS, which marks the closure of Bangong Tethys during the Mesozoic (Kapp & DeCelles, 2019; Yin & Harrison, 2000; Zhu et al., 2013). Upper Cretaceous (approximately 100 Ma) terrestrial molasse unconformably overlies older units in the southern Qiangtang subterrane, BNS, and northern Lhasa subterrane (Wang et al., 2013), and represent an overlap assemblage constraining the suturing of the terranes (Zhu et al., 2016).

South of the BNS (Figure 2a), the Lhasa Terrane is divisible into three subterranes based on zircon Hf isotope mapping with Archean basement in the central subterrane and Mesoproterozoic or younger crust in the northern and southern subterranes (Zhu et al., 2011). The minor exposures of Precambrian rock in the central subterrane are covered by widespread Permo-Carboniferous and Lower Cretaceous sedimentary rocks (Zhang et al., 2012; Zhu et al., 2013). The southern and northern subterranes consist of Triassic-Cretaceous strata (Wang et al., 2013), and their contacts with the central subterrane delineated by a fault (Luobadui-Milashan fault) and a mélange belt (Shiquan River-Nam Tso mélange), respectively (Figure 2a). The magmatic rocks in the central and southern subterranes range from 220 to 10 Ma (S.M. Li, Wang, et al., 2018; Zhu et al., 2019), whereas those in the northern subterrane are mainly Early Cretaceous (137–100 Ma; S.M. Li, Wang, et al., 2018).

North of the BNS (Figures 2a and 2b), the southern Qiangtang (SQ) subterrane is composed primarily of Upper Carboniferous to Middle Permian strata, with locally exposed pre-Devonian rocks (Pullen et al., 2011). Archean basement is inferred based on zircon Hf isotopes from Mesozoic and Cenozoic intermediate-felsic rocks (J.X. Li, Qin, et al., 2014; S.M. Li, Zhu, et al., 2014). The Mesozoic strata include Upper Triassic carbonates, Jurassic limestone and sandstone, and Lower Cretaceous volcano-sedimentary rocks (Kapp & DeCelles, 2019; Zhu et al., 2016). In the eastern SQ (Figure 2b), Jurassic sedimentary units are widespread, including from older to younger the Quse, Sewa, Buqu, Biluoco, Suowa, Daoban (also termed 114 Daoban), and Xiali formations (L. Li, Fan, et al., 2019; Ma et al., 2017; Wang et al., 2013). Jurassic igneous rocks have not been reported in this region. In the western SQ (Figure 2b), the Jurassic sedimentary units, which from older to younger are the Sewa, Shaqiaomu, and Jiebuqu formations, are distributed along the southern margin between the BNS and the extensive Jurassic intrusions (170–148 Ma; J.X. Li, Qin, et al., 2014).

The BNS extends over 1,200 km from east to west and has an across-strike width varying from 10 to 130 km (Figure 2b; Pan et al., 2004; Zhu et al., 2016). In the eastern segment, the Amdo microterrane (Kapp & DeCelles, 2019; also termed the Amdo microcontinent; Zhu et al., 2013) is bounded by mélange belts (Figure 2b). This microterrane is composed primarily of Neoproterozoic to early Paleozoic orthogneisses (920–820 and 540–460 Ma; Zhang et al., 2012; Guynn et al., 2012) and Early-Middle Jurassic intrusive rocks (194–173 Ma; Liu, 2012; Yan et al., 2016). The BNS contains the Mugagangri Group, tectonically disrupted ophiolitic fragments (Cheng & Xu, 1987), and Cretaceous igneous rocks (Fan et al., 2018). Paleozoic, Triassic, and Jurassic strata occur in the eastern segment in the Beila-Nagqu region. The Mugagangri Group is a greenschist-facies schistose unit characterized by heterogeneous blocks of sandstone, limestone, and volcanic rock in a highly deformed slate and fine sandstone matrix (Kapp et al., 2003, 2005, 2007; Wang et al., 2013; M. Zeng, Zhang, et al., 2016). It is unconformably overlain by the Upper Jurassic Shamuluo formation (Wang et al., 2013; Li, Guilmette, et al., 2017). The ophiolites are well exposed and comprise various ultramafic and mafic rocks, as well as cherts (B.D. Wang, Wang, et al., 2016). The mafic rocks from these ophiolites are dated mostly at 190–180 and 170–160 Ma (Tang, Zhai, Hu, Xiao, et al., 2018). Early Cretaceous (120–110 Ma) mafic rocks are basalts and gabbros without peridotites, and are exposed as blocks within mélange (Fan et al., 2018). Early Cretaceous granitoids and felsic volcanic rocks (Qushenla formation, 125–110 Ma) are widespread within the BNS (Fan et al., 2018; Wu et al., 2018).

3. Regional Setting, Sampling, and Analytical Methods

The segment of the BNS investigated in this study is in the Beila-Dongqiao region (Figure 2c) and has a N-S width of approximately 130 km and includes Paleozoic carbonates and Triassic sandstones exposed along the flanks, as well as locally in the central part, of the suture zone. Jurassic strata and mélange (Wang et al., 2013) are the primary units in this area and are in fault contact with Paleozoic and Triassic strata. Jurassic-Cretaceous intrusions and volcanic rocks are extensive within the BNS (Figure 2c). Jurassic sedimentary units can be subdivided into three E-W trending units (Figures 2c and 2d; Wang et al., 2013). (1) The Beila-Nagqu mélange belt is the southernmost belt of the suture zone. It separates the Lhasa Terrane to the south and the BNS to the north. It consists of flysch and ophiolitic fragments as well as limestone blocks (tens of meters in length) in a sandstone matrix. The ophiolitic mafic rocks are dated at approximately 190 Ma (Kong et al., 2017), 172–159 Ma (X.C. Wang, Xia, et al., 2018; Tang et al., 2018), and approximately 148 Ma (Zhong, Liu, et al., 2017). (2) The Jienu Group and conformably underlying Xihu Group in the

Table 1
Summary of Sample Locations, Petrographical Features, Zircon U–Pb Ages, and SiO_2 of the Igneous Rocks and Sandstones in the Beila-Dongqiao Section of the Bangong-Nujiang Suture

Label	Lithology	Latitude	Longitude	Age ± 2σ (Ma)	SiO_2	Petrographic characteristics
15DRC02	Andesite	N31°38.235′	E90°47.528′	164.1 ± 0.9	60.70	Porphyritic texture with main phenocryst phase of plagioclase and minor phase of amphibole and biotite
15DRC01	Dacite	N31°38.235′	E90°47.528′	163.6 ± 0.7	63.80	
15DRC13	Dacite	N31°38.251′	E90°47.571′	166.0 ± 0.6	64.65	
15JQ07	Dacite	N31°41.839′	E90°34.244′	165.0 ± 0.8	65.20	
13BG02-1	Rhyolite	N31°36.472′	E90°56.568′	163.9 ± 1.1	75.06	Porphyritic texture with phenocryst dominated by quartz and minor biotite
15JQ20	Rhyolite	N31°40.116′	E90°34.248′	164.9 ± 0.6	77.51	
14JC04-1	Granodiorite	N31°34.181′	E90°54.318′	166.5 ± 1.1	64.44	Medium-grained granitic texture; Pl (40–45%), Hb (10–15%), Kfs (15–20%), Qtz (10–15%), Bi (5–10%)
13BG01-1	Monzogranite	N31°33.556′	E90°55.586′	163.1 ± 1.0	73.70	Fine- to medium-grained granitic texture; Qtz (40–45%), Kfs (35–40%), Pl (10–15%), Bi (<5%)
15PC02	Granodiorite porphyry	N31°35.266′	E91°00.190′	113.6 ± 0.4	66.18	Porphyritic texture with plagioclase phenocryst
15PC08	Rhyolitic tuff	N31°43.181′	E91°00.975′	112.6 ± 0.6	76.72	Ignimbrite texture with quartz phenocryst
15JQ15	Rhyolite	N31°40.507′	E90°34.492′	114.4 ± 0.7	76.77	Porphyritic texture with main phenocryst phase of quartz and minor phase of biotite and plagioclase
15JQ17	Rhyolite	N31°40.508′	E90°34.492′	114.2 ± 0.8	75.66	

Label	**Lithology**	**Latitude**	**Longitude**	**Units**	**Petrographic characteristics**
18BL17-2	Sandstone	N31°29.196′	E90°50.400′	Beila-Nagqu mélange	Feldspatho-quartzo-lithic sandstone, lithic fragments are dominated by volcaniclastic
15JC01	Sandstone	N31°43.377′	E90°33.407′	Blocks in Daru mélange	Litho-quartzose sandstone, lithic fragments are sandstone and chert
15JC02		N31°43.377′	E90°33.407′	Blocks in Daru mélange	
15JC09		N31°41.840′	E90°34.244′	Blocks in Daru mélange	
15PC01	Sandstone	N31°35.895′	E91°00.144′	Jienu Group	Quartzo-lithic sandstone, lithic fragments are volcaniclastic, chert, limestone, sandstone
15PC05		N31°41.177′	E91°06.832′	Jienu Group	
15PC11	Sandstone	N31°52.549′	E90°55.370′	Dongqiao-Amdo mélange	Litho-quartzose sandstone, lithic fragments are volcaniclastic
15BA06	Sandstone	N32°27.559′	E91°48.282′	Daoban formation	Litho-quartzose sandstone, monocrystalline quartz; minor K-feldspar and plagioclase
15BA07		N32°26.475′	E32°26.475′	Daoban formation	

central part of the BNS zone are composed primarily of shale interbedded with sandstone. There is a second group of exposures of mélange and ophiolites, locally preserved between Daru Tso and Peng Tso (Figures 2c and 2d) and in fault contact with the Jienu and Xihu groups, which we term Daru Tso mélange. The mélange contains sandstone blocks (tens of centimeters to several meters) in shale matrix, and ophiolitic fragments. The age of the ophiolites within the Daru Tso mélange is approximately 188 Ma (Huang et al., 2015). (3) The Dongqiao-Amdo mélange belt is in the northernmost part of the BNS and is bounded to the north by the SQ (Figures 2c and 2d). It consists of limestone blocks (several kilometers in length) within a sandstone matrix and ophiolitic fragments of variable sizes (several centimeters to tens of meters) in fault contact with the matrix. The ophiolitic mafic blocks are dated at 190–180 Ma (B.D. Wang, Wang, et al., 2016; Liu et al., 2016). This northernmost belt is overlain across an angular unconformity by the Upper Jurassic Shamuluo formation, which is a coherent succession of limestone and sandstone.

In this study, we investigated both igneous and sedimentary rocks around the Beila-Dongqiao section of the suture zone. Table 1 lists petrographic observations, and Figure 3 shows field photos and photomicrographs. For the igneous rocks, zircon U-Pb dating was undertaken on 12 samples, which display oscillatory zoning under cathodoluminescence (CL) imaging. For each sample, 18–30 spots were analyzed and the U-Pb data were divisible into two age groups (166–163 and 114–112 Ma). Geochemical compositions and zircon Hf-O isotopes of samples from the older group, which is the focus of this study, were also determined. For the nine sandstone samples, both rim and core of detrital zircons as determined by CL imaging were analyzed with 100–140 spots for each sample. All zircon U-Pb isotopes were analyzed via laser ablation-inductively coupled plasma mass spectrometry, following the methods described in Zhang et al. (2019). U-Pb data off-line analysis follows Andersen (2002), Ludwig (2003), and Liu et al. (2010). We follow the methodology of Liu et al. (2008) for major and trace element analysis, Brach-Papa et al. (2009) for Sr isotopes, and Gaffney

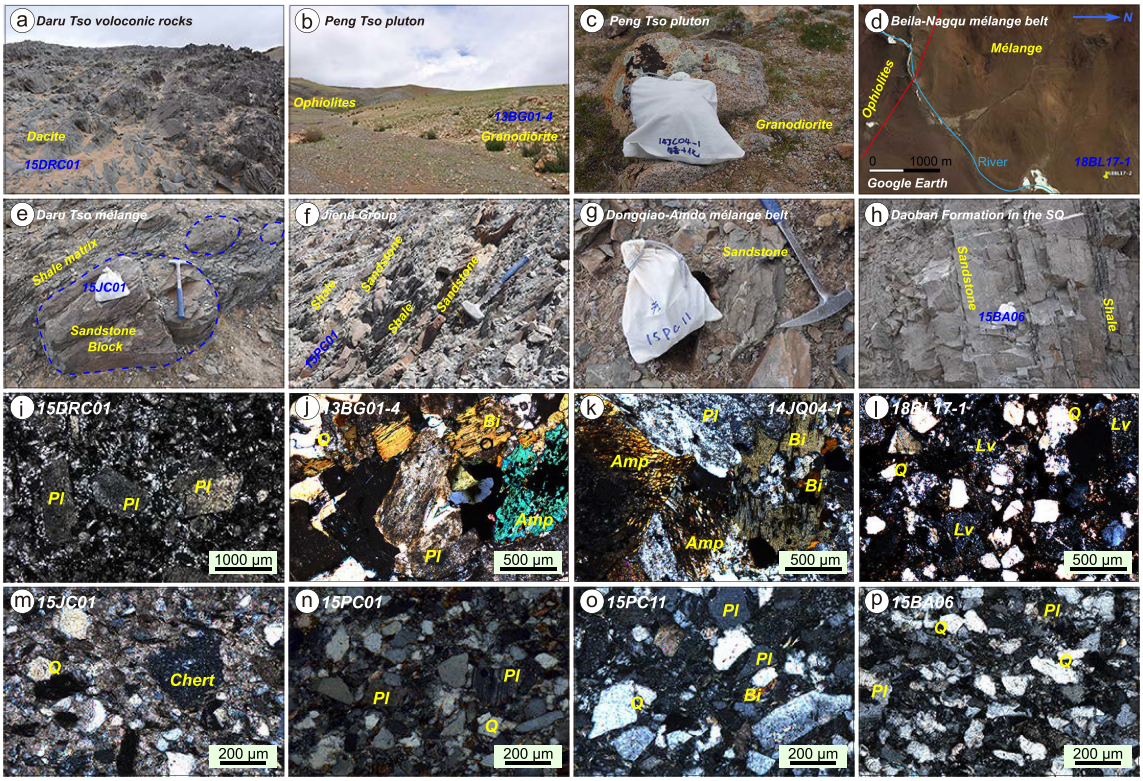

Figure 3. Representative field photographs and photomicrographs for (a–c and i–k) various magmatic rocks, respectively, and (d–h and l–p) mélange and sedimentary rocks, respectively. Abbreviations: Q = quartz, Pl = plagioclase, Amp = amphibole, Bi = biotite, Lv = volcanic fragments.

et al. (2007) for Nd isotopes. Zircon O isotopic composition was analyzed before in situ U-Pb dating using secondary ion mass spectrometry following the methods in Yang et al. (2018). In situ Hf isotope analyses were performed using laser ablation-inductively coupled plasma mass spectrometry and methods in Liu et al. (2010).

4. Results

4.1. Zircon U-Pb Ages

4.1.1. Magmatic Rock Ages

Zircon grains are subhedral to euhedral prismatic crystals with lengths of 50–200 μm and are mostly oscillatory zoned with no inherited cores visible in CL images. Dated spots show varying abundances of Th (46–5,842 ppm) and U (113–2,748 ppm), and Th/U ratios of 0.20–6.74 (Table S1). These characteristics are typical of zircons from igneous rocks. Figure 4 displays the zircon U-Pb concordia plots and results of weighted mean $^{206}Pb/^{238}U$ ages, the number of analyzed spots (n), and the mean square of the weighted deviation (MSWD). Twelve samples define two periods of activity with eight samples dated at 166–163 Ma and four samples dated at 114–112 Ma.

4.1.2. Detrital Zircon Ages From Sandstone Samples

Representative CL images and concordia plots of analyzed zircons from sandstone samples are shown in Figures S1 and S2 in the supporting information. The age-distribution diagram (relative age probability) for each of the nine samples is shown in Figure 5. Zircon grains from sandstones are subhedral to occasionally rounded with length-to-width ratios of 1:1 to 4:1 and lengths of 40–150 μm. Most zircons exhibit planar zoning or oscillatory zoning, and a few display core-rim structures (Figure S1). Ages with >10% discordance and >5% reverse discordance are not included (Figure S2), and 994 analyses yield 860 usable ages (Table S2). The shorthand YC1σ(2+) stands for the mean age of the youngest age group with two or more grains overlapping in age at 1σ (Dickinson & Gehrels, 2009). It is generally interpreted as the maximum depositional age of strata. The results of nine samples from five units are described from south to north below.

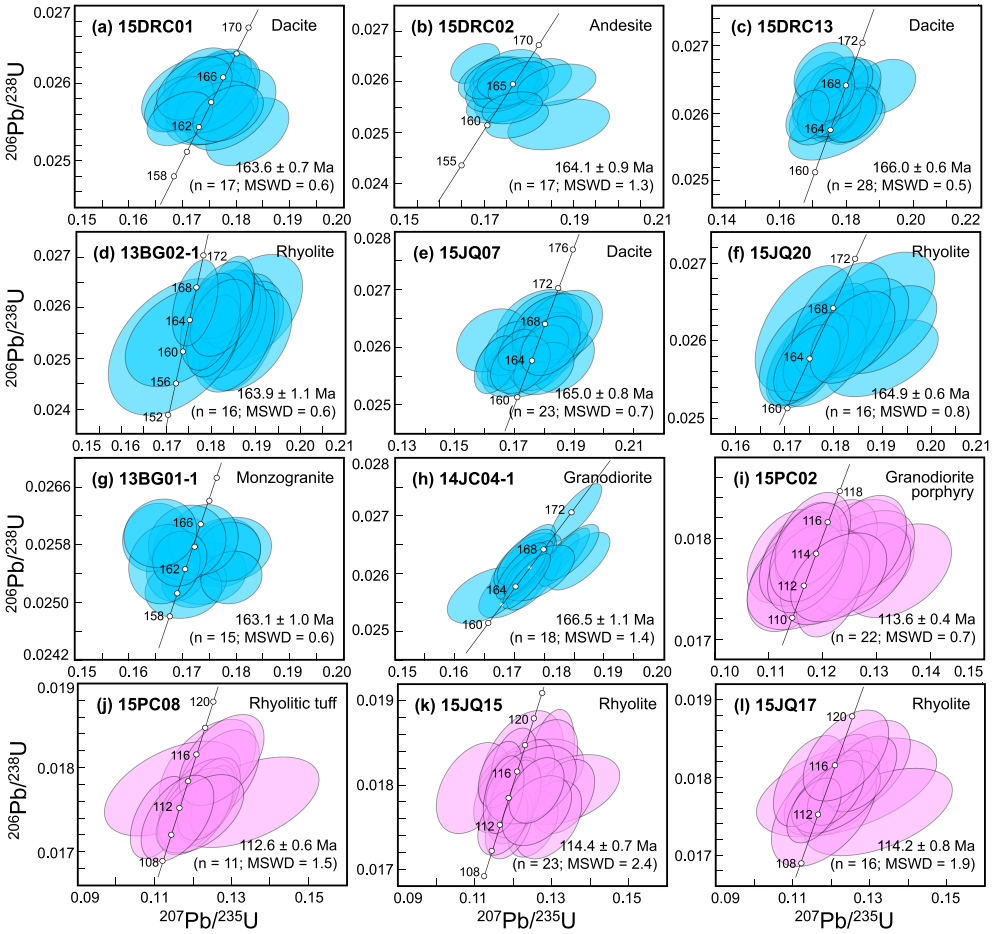

Figure 4. Zircon U-Pb concordia diagrams for the igneous rocks.

1. Beila-Nagqu mélange belt: Age distributions for sample 18BL17-2 are characterized by the presence of a marked peak at approximately 166 Ma (168–162 Ma, $n = 16$, 12% of analyses, YC1σ(2+) = 166 ± 1 Ma) and the absence of the 350–200 and 194–170 Ma age populations. Older age clusters occur at 580–500 Ma (17%), 1,000–860 Ma (17%), 1,050–1,150 Ma (15%), and 2.6–2.4 Ga (5%).
2. Daru Tso mélange: Three samples of blocks within the mélange (15JC01, 15JC02, and 15JC09) display similar age distributions. A compiled result from three samples reveal ages ranging from 3,170 to 204 Ma, with age groups for 304 analyses at 350–204 Ma (22%), 2.0–1.8 Ga (19%), 520–400 Ma (12%), 850–700 Ma (12%), and 2.6–2.4 Ga (7%). They are characterized by the absence of Jurassic ages with YC1σ(2+) of 205 ± 3 Ma ($n = 2$).
3. Jienu Group: Dominant age populations of 186 analyses (compiled results) for two samples 15PC05 and 15PC01 occur at 350–200 Ma (24%) and 2.0–1.8 Ga (22%) and subordinate age populations occur at 2.6–2.4 Ga (10%), 850–700 Ma (10%), 460–390 Ma (7%), and 1,000–900 Ma (5%). These two samples yield YC1σ(2+) of 236 ± 3 Ma ($n = 2$) and 170 ± 1 Ma ($n = 2$), respectively.
4. Dongqiao-Amdo mélange belt: Detrital zircons of one matrix sample 15PC11 show age patterns analogous to those of Jienu Group. It has age clusters at 350–200 Ma (25%), 2.0–1.8 Ga (16%), 2.6–2.4 Ga (9%), 450–390 Ma (5%), and 180–176 Ma (5%). The YC1σ(2+) is 176 ± 2 Ma ($n = 3$), slightly older than those of Jienu Group.
5. Daoban formation in the SQ: Combined ages for samples 15BA06 and 15BA07 range from 2,777 to 159 Ma. One-hundred-and-fifty-eight analyses yield significant age groups at 2.0–1.8 Ga (24%) and 350–200 Ma (22%) and subordinate age groups at 2.6–2.4 Ga (12%), 185–159 (11%), 820–780 Ma (6%), and 470–410 Ma (5%). The Jurassic ages of these two samples are similar, yielding a YC1σ(2+) of 166 ± 2 Ma ($n = 5$).

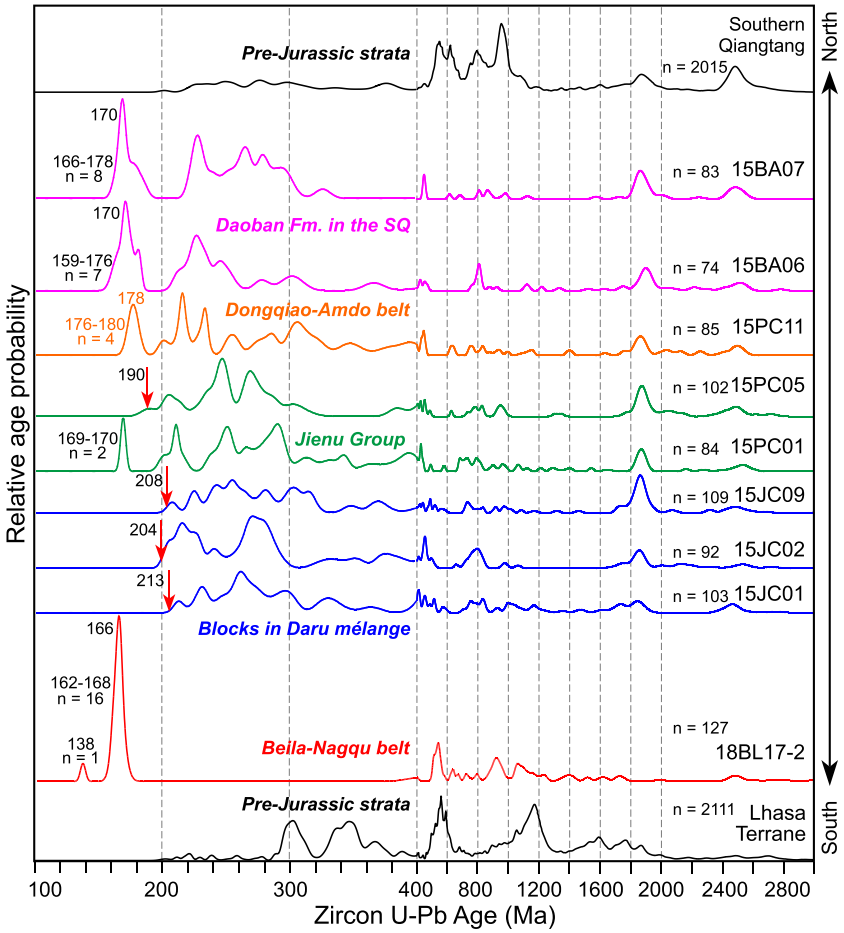

Figure 5. Relative age probability diagram of detrital zircons of sandstones from mélange and Jurassic strata in the BNS and SQ, compared to those of the pre-Jurassic strata in the Lhasa Terrane (Dong et al., 2010; Cai et al., 2016; Gehrels et al., 2011; Guo et al., 2016, 2017; G. Li, Sandiford, et al., 2014; Zhu et al., 2011) and the SQ (Dong et al., 2011; Fan et al., 2015; Gehrels et al., 2011; Ma et al., 2017; Pullen et al., 2008, 2011; M. Wang, Li, et al., 2016, Wang, Peng, et al., 2018; Zhu et al., 2011).

4.2. Geochemical Compositions and Isotopes of Middle Jurassic Magmatic Rocks

The Middle-Late Jurassic igneous rocks (166–163 Ma) include granitoids and volcanic rocks. Petrographic observations (Figure 3) indicate that granitoids experienced minor degrees of alteration, whereas the volcanic rocks experienced generally greater degrees of alteration to form secondary sericite, smectite, and chlorite. This is consistent with the loss on ignition results of 0.5–1.1 and 2.9–8.1 wt %, respectively (Table S3). Major element analyses have been recalculated to volatile-free for all rocks. Only rare earth elements and high field strength elements, which are generally immobile trace elements, are used for discussion of the volcanic rocks.

4.2.1. Granodiorites and Monzogranites

The granodiorites and monzogranites (SiO_2 = 64.4–73.7 wt %) around Peng Tso (Figure 2c) have high total alkalis ($K_2O + Na_2O$ = 7.4–8.5 wt %), low FeO^T/MgO (2.0–3.9; Figure 6a), and high K_2O (4.1–5.5 wt %; Figure 6b). These samples are high-K calc-alkalic series and are metaluminous with aluminum saturation index of 0.95–1.03. These samples are characterized by low MgO of 0.5–2.8 wt % (Figure 6c), Mg# of 32–48 (Figure 6d), and P_2O_5 of 0.07–0.16 (Table S3). On Harker diagrams, major element contents typically show inverse correlation trends with silica from granodiorite to monzogranite. These rocks are enriched in Th, U, and light rare earth elements and are depleted in Nb, Ta, Eu, and Ti (Figures 6e and 6f).

Granodiorite samples 13BG01-4 and 14JC04-1 yield evolved Sr-Nd isotopic compositions with $(^{87}Sr/^{86}Sr)_i$ of 0.70704 to 0.70773, $\varepsilon_{Nd}(t)$ values of −8.2 to −7.5 (Figure 7a), and two-stage Nd model ages (T_{DM2}) of

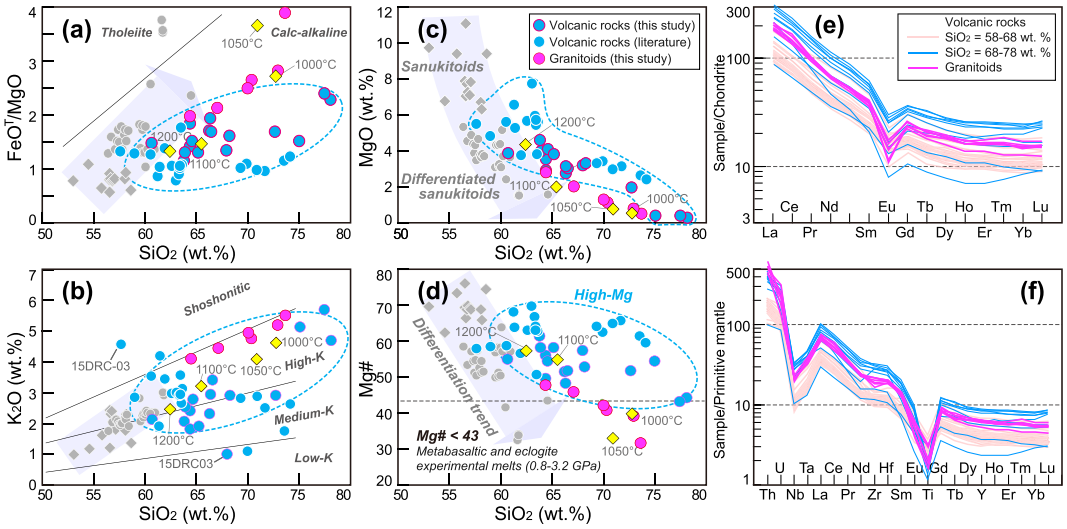

Figure 6. Diagrams for 166–160 Ma igneous rocks. (a) Plots of FeO^T/MgO versus SiO_2 (Miyashiro, 1974) and (b) K_2O versus SiO_2 (Le Maitre, 2002) for classification. (c) Plots of MgO versus SiO_2 and (d) Mg# versus SiO_2. The field for the metabasaltic and eclogite experimental melts (0.8–3.2 GPa) are from Rapp et al. (1999), and references therein. Sanukitoids and differentiated sanukitoids (Tatsumi, 2006) are showed for contrast. The yellow diamonds stand for experimental melts of MORB-sediment mélange melting at temperatures of 1,000–1,200 °C (Castro et al., 2010). (e) Chondrite-normalized REE and (f) primitive-mantle-normalized trace element (values from Sun and McDonough (1989)) diagrams.

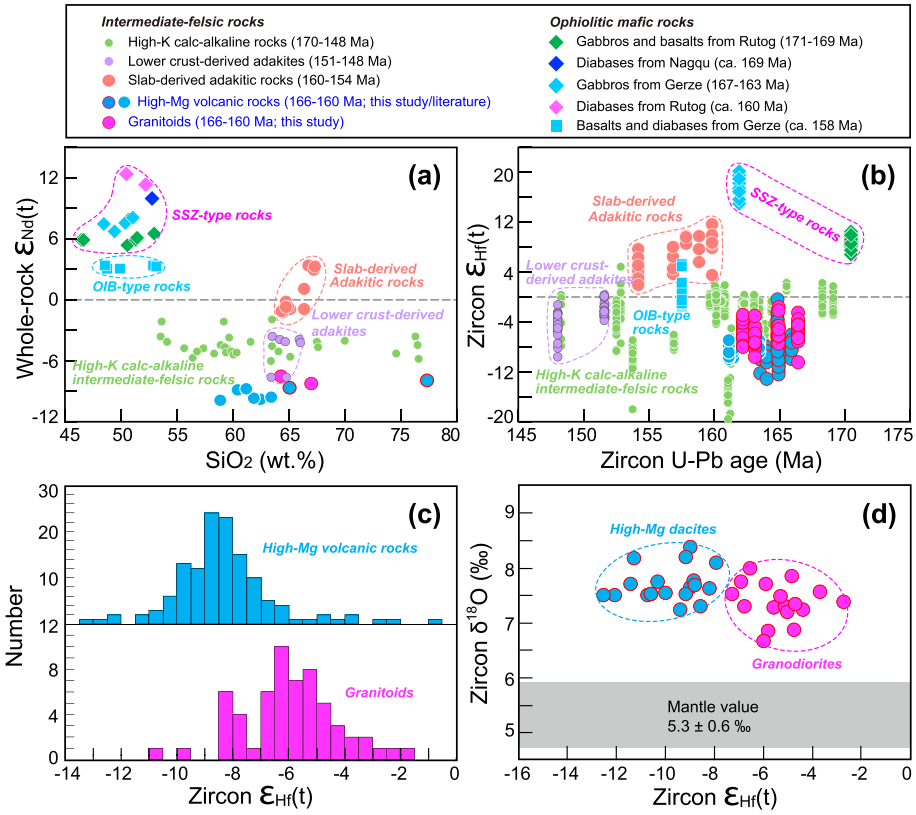

Figure 7. (a) Whole-rock $\varepsilon_{Nd}(t)$ versus SiO_2 and (b) zircon $\varepsilon_{Hf}(t)$ versus zircon U-Pb ages for the 170–148 Ma igneous rocks and 170–160 Ma ophiolitic mafic rocks in the SQ and BNS. See Tables S5 and S7 for data sources. (c) Zircon $\delta^{18}O$ versus zircon $\varepsilon_{Hf}(t)$ for the Daru Tso 166–160 Ma igneous rocks (dacite 15JQ07 and granodiorite 14JC04-1).

1.62–1.56 Ga. Granodiorite samples 13BG01-4 and 14JC04-1 and monzogranite samples 13BG01-1 and 13BG04-1 have analogous zircon $\varepsilon_{Hf}(t)$ values of −10.6 to −1.8 (Figures 7b and 7c), with Hf isotope crustal model ages (T_{DM}^{C}) of 1.86–1.30 Ga. The zircon $\delta^{18}O$ values for granodiorite sample 14JC04-1 are 6.7‰ to 8.0‰ (Figure 7d and Table S4).

4.2.2. Andesites, Dacites, and Rhyolites

The volcanic rocks were collected from Jiaqun via Daru Tso to Peng Tso (Figure 2c). All these rocks show similar geochemical signatures with SiO_2 ranging from 60.7 to 78.1 wt % and thus are classified as andesites, dacites, or rhyolites. All volcanic rocks have low FeO^T/MgO (1.1–2.4; Figure 6a) and are calc-alkaline rocks. These samples belong to high-K series (Figure 6b), as is also indicated by the Th versus Co plot used for the classification of altered rocks (Figure S3; Hastie et al., 2007) with high Th of 8.7–41.4 ppm. These volcanic samples are characterized by high MgO and Mg# (Figures 6c and 6d) and are termed high-Mg andesites, dacites, and rhyolites. Their MgO (0.3–4.5 wt %) and Mg# (43–61) are higher than those of typical arcs (Wang et al., 2014), experimental melts of metabasalts and eclogites (Rapp et al., 1999, and references therein) at similar SiO_2 contents. The high-Mg volcanic rocks share similar trace element signatures (Figures 6e and 6f) with the granitoids. The trace element abundances for volcanic rocks decrease from andesites to dacites to rhyolites, with similar chondrite-normalized $(La/Yb)_N$ ratios of 10.4, 7.2–12.4, and 9.4–24.8, respectively.

One dacite sample 15JQ07 and one rhyolite sample 15JQ20 were analyzed for Sr-Nd isotopic compositions, yielding $(^{87}Sr/^{86}Sr)_i$ of 0.70766 and 0.70639, $\varepsilon_{Nd}(t)$ values of −8.6 and −7.9 (Figure 7a), and T_{DM2} of 1.65–1.59 Ga. Zircons $\varepsilon_{Hf}(t)$ values for andesite sample 15DRC02 are −13.3 to −8.2, for dacite samples 15DRC01 and 15JQ07 are −12.5 to −7.9, and for rhyolite samples 13BG02-1 and 15JQ20 are −10.0 to −0.5 (Figures 7b and 7c). These volcanic rocks have T_{DM}^{C} of 2.03–1.22 Ga. One dacite sample 15JQ07 yield zircon $\delta^{18}O$ values of 7.2‰ to 8.4‰ (Figure 7d and Table S4).

5. Discussion

Below we discuss our results and those of others for understanding the Jurassic igneous (section 5.1) and sedimentary (section 5.2) rocks in the eastern BNS. Based on these interpretations, a Middle-Late Jurassic convergent margin (section 5.3) with an overall compressional setting (section 5.4) is established along the strike (approximately 1,200 km) of the BNS and SQ. We evaluate the existing interpretations for the Middle-Late Jurassic geological record within the BNS and SQ and propose a model involves subparallel ridge subduction (section 5.5).

5.1. Petrogenesis of Middle-Late Jurassic Igneous Rocks

Data reported here and published previously (X. Li et al., 2015; H.F. Li, Liu, et al., 2019; Y.C. Zeng, Chen, et al., 2016) suggest that a Middle-Late Jurassic (166–160 Ma) magmatic belt existed around the Daru Tso. These rocks are high-K calc-alkaline intermediate-felsic rocks (Figures 6a, 6b and S4) and are metaluminous (Table S3), including granitoids and high-Mg andesites, dacites, and rhyolites.

The Peng Tso granitoids studied here are I-type rocks as indicated by the presence of amphibole (Figures 3j and 3k; Chappell, 1999), low aluminum saturation index of 0.95–1.03 (Chappell, 1999), and low abundances of high field strength elements (Whalen et al., 1987), for example, Zr (183–240 ppm) and Nb (13.6–16.4 ppm; Table S3). The I-type granites are interpreted as partial melting of the meta-igneous lower crust (Chappell, 1999; Chappell & White, 2001). The Peng Tso granitoids could be generated by partial melting of an ancient lower crust as implied by the evolved isotopes ($\varepsilon_{Nd}(t) = -8.2$ to −7.5; zircon $\varepsilon_{Hf}(t) = -10.6$ to −1.8; Figures 7a and 7b), the Nd T_{DM2} (1.62–1.56 Ga), and Hf T_{DM}^{C} (1.86–1.30 Ga). These model ages indicate that they either originated from anatexis of Proterozoic crust or through anatexis of Archean crust with input of mantle-derived magmas. Both these possibilities are consistent with the high zircon $\delta^{18}O$ values (6.7‰ to 8.0‰; Figure 7d). The evolutionary trend on the Harker diagrams (Figures 6b and 6c) indicates that the monzogranites were produced by fractionation of granodioritic magmas.

Compared with the Peng Tso granitoids, the andesites, dacites, and rhyolites (SiO_2 = 58–78 wt %) are characterized by higher MgO (2.4–7.7 wt %; Figure 6c) and the compatible elements Cr (1.4–395 ppm) and Ni (1.8–213 ppm), and by lower zircon $\varepsilon_{Hf}(t)$ of −13.3 to −0.5 (Figures 7a and 7b). These signatures require involvement of both mantle and sediments via modification of mantle peridotites by sediment melts

(Stern, 2002; Tatsumi, 2006), magma mixing (Kemp et al., 2007), and partial melting of mélange diapirs (Marschall & Schumacher, 2012; Nielsen & Marschall, 2017). The first two processes are considered unlikely. Partial melting of mantle wedge metasomatized by subducted sediment melts (Stern, 2002) would generally generate high-Mg basaltic to andesitic magmas and low-Mg andesitic to dacitic magmas, for example, the sanukitoids (SiO_2 = 53–58 wt %) and differentiated sanukitoids (SiO_2 = 56–65 wt %), respectively, from Setouchi, southwest Japan (Tatsumi, 2006). Both differ from the high-Mg andesitic to rhyolitic rocks in this study (Figures 6c and 6d). Magma mixing between sediment-derived magmas and mantle-derived magmas (Kemp et al., 2007) would generate a depleted trend for isotopic compositions from rhyolites to andesites. However, the rhyolites ($\varepsilon_{Nd}(t) = -7.9$; zircon $\varepsilon_{Hf}(t) = -10.0$ to -0.5) show similar $\varepsilon_{Nd}(t)$ and higher zircon $\varepsilon_{Hf}(t)$ than those of the andesites ($\varepsilon_{Nd}(t) = -9.7$ to -8.7; zircon $\varepsilon_{Hf}(t) = -13.3$ to -8.2; Figure 7b and Tables S3 and S4). The high-Mg intermediate-felsic rocks could be generated by partial melting of mélange diapirs in the mantle wedge where sediments, altered oceanic crust, and ultramafics have physically mixed (Castro et al., 2010; Codillo et al., 2018; Gerya & Yuen, 2003), for example, in the North Volcanic Province of Colombia (Errázuriz-Henao et al., 2019) and in the western Trans-Mexican Volcanic Belt (Parolari et al., 2018). A sediment-dominated mélange (Castro & Gerya, 2008) is consistent with the evolved isotopic compositions of the volcanic rocks in this study (Figures 7a and 7b). The interaction between ascending mélange-derived magmas and mantle wedge peridotites would yield high MgO and Mg# (McCarron & Smellie, 1998; Parolari et al., 2018).

The granitoids and high-Mg volcanic rocks could be generated by partial melting of lower crust and mélange diapirs, respectively. These rocks are widespread above subduction zones (Lee et al., 2007; Nielsen & Marschall, 2017; Castro, 2019), indicating the development of what we term the Daru Tso arc (Figure 2c).

5.2. Provenance Analysis and Depositional Age of Sedimentary Units

Pre-Jurassic detrital zircons from sedimentary units within the BNS and from the Daoban formation in the SQ display similar age spectra, with peaks at approximately 2.5 Ga, 1.85 Ga, and 440 Ma (Figure 5). The zircons also show an age cluster at 350–200 Ma except those from the Beila-Nagqu mélange belt. All these peaks are typical in the Jurassic strata in the eastern SQ (e.g., Middle Jurassic Sewa formation; Ma et al., 2017) and some of these peaks can be observed in pre-Jurassic strata in the SQ to the north (e.g., the approximately 1.85 Ga and approximately 960 Ma; Gehrels et al., 2011; Zhu et al., 2011). These are different from those of pre-Jurassic strata in the Lhasa Terrane to the south, which show peaks at approximately 1,170, 350, and 300 Ma (Gehrels et al., 2011; G. Li, Sandiford, et al., 2014; Zhu et al., 2011). Therefore, all units in this study exhibit a SQ affinity (Figure 5).

Jurassic detrital zircons with ages of 190–169 and 168–159 Ma in sandstones studied here can be linked to the Amdo microterrane magmatic rocks (194–173 Ma; Figure 1b; Liu, 2012; Yan et al., 2016) and the Daru Tso arc (166–160 Ma; Figure 2c) within the BNS. The southernmost Beila-Nagqu mélange belt, lying to the south of the Daru Tso arc, was sourced from the Daru Tso arc but not from the Amdo magmatic rocks. This is indicated by the presence of 168–162 Ma detrital zircons and the absence of 194–170 Ma detrital zircons (Figure 5). The maximum depositional age of this unit is approximately 166 Ma as indicated by the YC1σ(2+) of 166 $\pm$ 1 Ma (n = 16). To the north of the Daru Tso arc, the Jienu Group and Dongqiao-Amdo mélange belt within the BNS (Figure 2c) were likely deposited during the Middle Jurassic (approximately 170 Ma) as constrained by the YC1σ(2+) of 170 $\pm$ 1 Ma (n = 2) and 176 $\pm$ 2 Ma (n = 3), respectively, and the absence of approximately 166–160 Ma zircons. These two units were likely sourced from the adjacent Amdo arc-related magmatic rocks (194–173 Ma; Liu, 2012; Yan et al., 2016) as implied by the presence of the 190–169 Ma detrital zircon age populations (Figure 5). Further to the north, the Daoban formation in the SQ has a maximum depositional age (YC1σ(2+)) of 166 $\pm$ 2 Ma (n = 5) and Jurassic detrital zircons ranging in age from 185 to 159 Ma. These ages likely reflect recycling from the underlying Sewa formation (Ma et al., 2017) and/or from the Amdo magmatic rocks for the 185–170 Ma zircons and the Daru Tso magmatic belt for the 168–159 Ma zircons.

5.3. Identification of a Single Middle-Late Jurassic Arc-Trench System

Our new geochronological and geochemical data, along with existing data (Hu et al., 2017; Wu et al., 2018), reveal a Daru Tso arc (166–160 Ma) covering approximately 40 km in E-W length and approximately 20 km in N-S width within the eastern BNS, which is followed by a magmatic gap (160–120 Ma) in the Beila-Nagqu

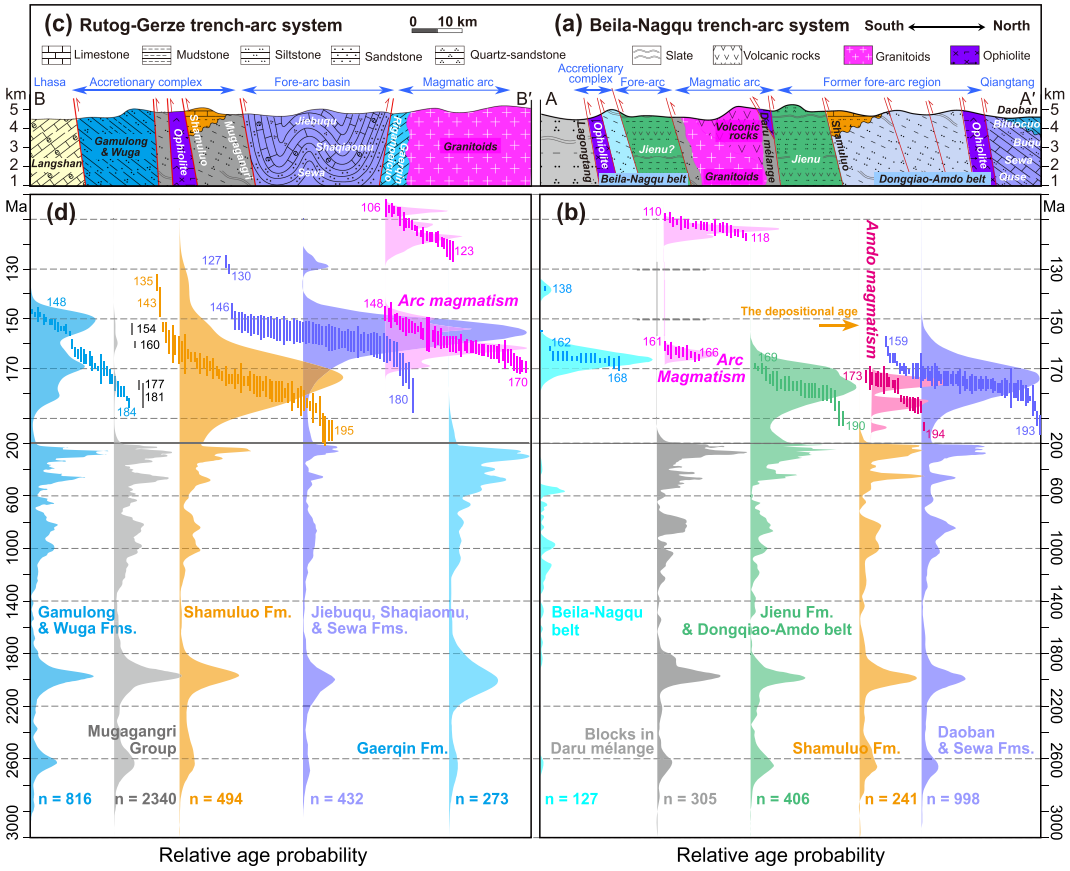

Figure 8. Simplified cross sections around (a) Beila and (c) Gerze. See Figure 2b for locations of these two sections. (b and d) Relative age probability diagram of detrital zircon from mélange and Jurassic strata along these two sections, as well as ages of Jurassic-Early Cretaceous magmatic rocks in the SQ, Amdo microterrane, and BNS. Data sources are given in section 5.3 and also in Tables S5 and S7 in the supporting information, which provides specific geological records of the Middle-Late arc-trench systems.

region (Figures 8a and 8b). The new detrital zircon ages indicate the development of contemporaneous sedimentary rocks to the south and north of the Daru Tso arc (Figure 5). These observations reveal the existence of the Beila-Nagqu arc-trench system (166–160 Ma) in the eastern segment of the BNS and SQ (Figures 8a and 8b), including from south to north Beila-Nagqu accretionary prism represented by the southernmost Beila-Nagqu mélange belt, Daru Tso arc within the BNS, and retro-arc sedimentary units represented by the Daoban (this study) and Xiali formations (L. Li, Fan, et al., 2019) in the SQ (Figures 2c and 8a). This arc-trench system built on a slightly older arc system (194–170 Ma) as implied by the presence from south to north of the coeval Dongqiao-Amdo mélange belt within the northernmost of the BNS (this study), Amdo arc-related magmatism (Figure 2b; Liu, 2012; Yan et al., 2016), and the Sewa formation in the SQ (Figure 8b; Ma et al., 2017).

The Beila-Nagqu arc-trench system was likely an extension of the Rutog-Gerze arc-trench system, which is documented by previous studies along strike of the western segment of the BNS and SQ (Figures 8c and 8d). The Rutog-Gerze arc-trench system was active from 170 to 148 Ma, and is interpreted to contain an accretionary prism represented by the Wuga and Gamulong formations along the southern margin of the BNS (Li, Guilmette, et al., 2017; Sun et al., 2018); a forearc basin consisting of the Sewa, Shaqiaomu, and Jiebuqu formations (Huang et al., 2016) in the southern margin of the SQ; and a broad Rutog-Gerze continental magmatic arc (J.X. Li, Qin, et al., 2014; Figures 1b and 8c) covering approximately 400 km in E-W length and approximately 130 km in N-S width in the SQ. This arc is succeeded by a prolonged magmatic gap (148–125 Ma).

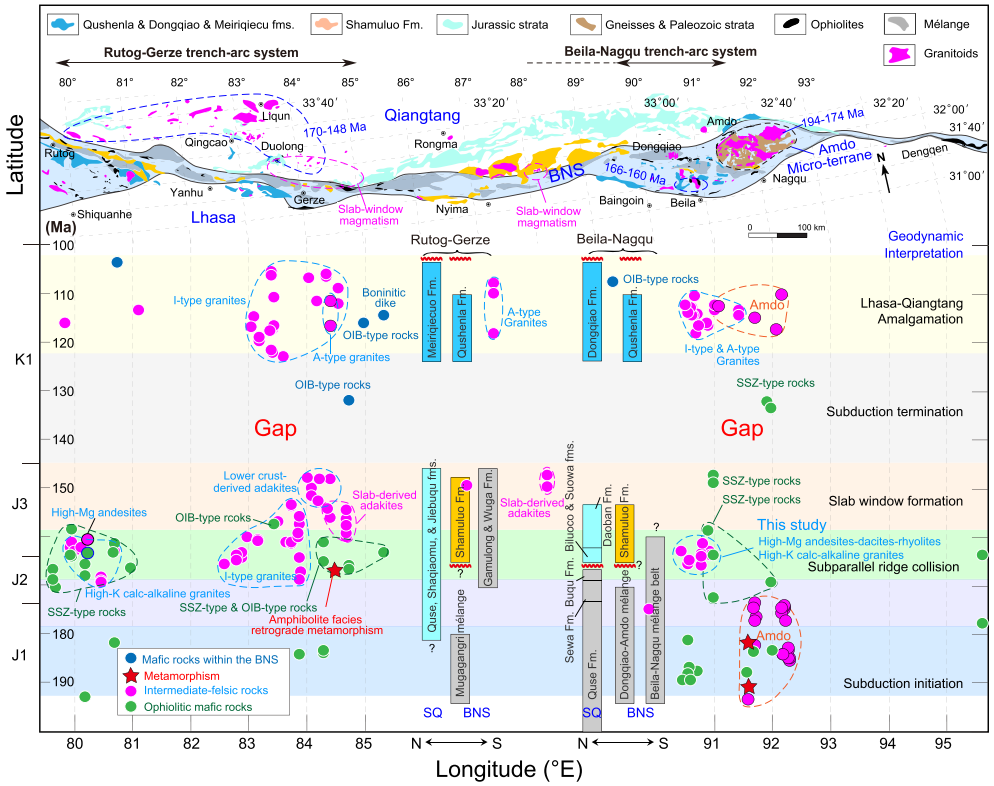

Figure 9. The time-space distributions of Jurassic-Cretaceous geological records, showing the Jurassic-Early Cretaceous magmatism, generation of ophiolites, metamorphism, sedimentation, and tectonism in the SQ, Amdo microterrane, and BNS. Data sources are listed in section 5.5.1 and Table S5, as well as from Zhu et al. (2016), Zhang et al. (2017), Zhong, Hu, et al. (2017), C. Li, Li, et al. (2018), and A. Ma, Hu, et al. (2018).

These observations reveal that a single arc-trench system developed above a north dipping subduction zone of the Bangong Tethyan lithosphere. This arc system can be divided into two distinct segments along the strike, which is characterized by magmatic activities of 166–160 Ma in the eastern and 170–148 Ma in the western segments, and is followed by magmatic gaps of 160–120 and 148–125 Ma, respectively.

5.4. A Pulse of Arc Uplift and Erosion During 166–160 Ma

Provenance analysis indicates that the Beila-Nagqu accretionary prism of the southernmost BNS and retro-arc Daoban formation in the SQ are sourced from the Daru Tso arc within the eastern BNS (166–160 Ma). Three lines of evidence imply that uplift and erosion of the arc is the cause of this sediment influx. First, paleogeographic reconstruction implies that the eastern SQ lay within a shallow-marine environment, whereas the eastern BNS, where the Daru Tso arc developed, lay in a deep-marine environment during Early-Middle Jurassic (~183–163 Ma; Ma et al., 2017; A. Ma, Hu, et al., 2018). Second, the 350–200- and 194–170-Ma detrital zircon age populations are absent from the Beila-Nagqu accretionary prism (Figure 5), but are present in sedimentary units lying to the north of the Daru Tso arc, for example, the Sewa (Ma et al., 2017) and Daoban (this study) formations (Figure 8b). This observation suggests that the Daru Tso arc formed a barrier preventing the transport of sediments from the SQ to the trench. Third, erosion of the arc will provide abundant volcanic fragments (Figure 3) and magmatic arc zircons (168–162 Ma, 12% of analyses; Figure 5) in sandstones from the Beila-Nagqu accretionary prism sandstones.

The uplift of Daru Tso arc is coeval with angular unconformities in the retro-arc regions (Figures 8a and 9) between the Shamuluo formation and underlying Dongqiao-Amdo mélange belt (at approximately 164 Ma; Wang et al., 2013) and between Biluoco and underlying Buqu formations (at approximately 166 Ma), based on fossil and detrital zircon ages (Ma et al., 2017; A. Ma, Hu, et al., 2018). Similar events have also been recognized in the forearc regions of the Rutog-Gerze arc-trench system (Figures 8c and 9) including rapid deposition of Gamulong conglomerates in a trench environment at approximately 166 Ma with poor

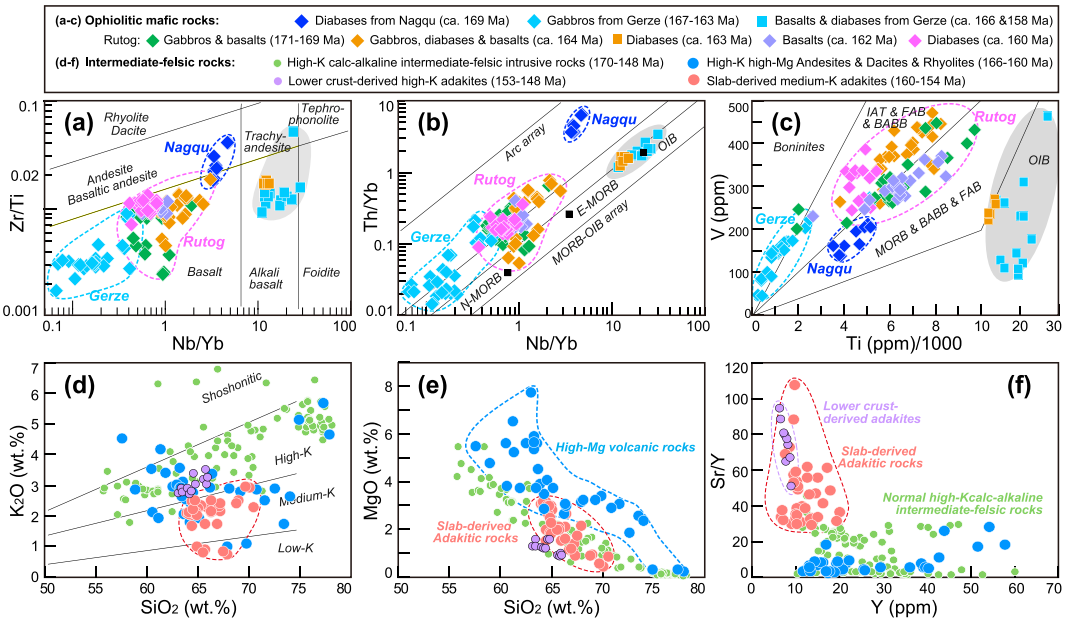

Figure 10. Classification diagrams for the Middle-Late Jurassic magmatic rocks in the SQ and BNS, including (a–c) ophiolitic mafic rocks (Pearce, 2014) and (d–f) intermediate-felsic rocks. Data source are same with the Figure 9 and are listed in Table S5.

grading and clast orientation (Sun et al., 2018) and the angular unconformity before approximately 153 Ma separating the Shamuluo formation from underlying Mugagangri Group (mélange; Li, Guilmette, et al., 2017), based on the youngest detrital zircon age clusters. These angular unconformities and rapid deposition are interpreted as indicators of a compressional setting (Ma et al., 2017; Li, Ding, et al., 2017; Sun et al., 2018).

5.5. Geodynamic Interpretation

5.5.1. Existing Geodynamic Models Proposed for Middle-Late Jurassic Geological Records

Figure 9 displays geological records during Jurassic and Early Cretaceous over 1,200 km along strike in the SQ and BNS. Four key observations, which must be accounted for in any geodynamic model, are emphasized here (Figure 9). (1) There are two stages of ophiolite formation at 190–180 Ma (Figure 9) and 170–160 Ma (Figures 10a–10c) along the BNS (Huang et al., 2017; Li et al., 2013; Liu et al., 2014; Liu et al., 2016; Shi, 2007; Shi et al., 2008; Tang, Zhai, Hu, Xiao, et al., 2018; B.D. Wang, Wang, et al., 2016; Zhong, Liu, et al., 2017), both of which are reported in the Beila-Nagqu area investigated in this study (Figure 9). (2) The convergent margin experienced an overall compressional setting from 166–160 Ma as inferred by an uplift of the Daru Tso arc, angular unconformities, and rapid deposition of trench deposits (section 4.4). (3) Slab window magmatism represented by slab-derived adakites (Figures 10d–10f) and OIB-type rocks (Figures 10a–10c) occurred around Gerze and Kangqiong during 160–148 Ma (S.M. Li, Zhu, et al., 2016; Y.L. Li, He, et al., 2016; Fan et al., 2016). (4) A magmatic gap extending from at least 148–125 Ma (Figure 9) is recognized in both the western (148–125 Ma; Fan et al., 2016, 2018; Li, Qin, et al., 2014; X. Li et al., 2015; S.M. Li, Zhu, et al., 2016; Y.L. Li, He, et al., 2016; Zhu et al., 2016) and eastern segments (160–120 Ma; this study; Hu et al., 2017; Wu et al., 2018), and is succeeded by extensive magmatism (125–105 Ma; Fan et al., 2015, 2018; Hao et al., 2016, 2018; J.X. Li, Qin, et al., 2014; Wu et al., 2018, 2019).

The Early Jurassic records are widely ascribed to northward subduction of the Bangong Tethys. The 190–180 Ma ophiolites along strike of the BNS (Figure 9) show suprasubduction zone (SSZ) signatures and are linked to subduction initiation (Liu et al., 2016; B.D. Wang, Wang, et al., 2016), as observed from the Izu-Bonin-Mariana forearc (Ishizuka et al., 2014; Stern et al., 2012). The Early Jurassic magmatic rocks (194–170 Ma; Figure 9; Liu, 2012; Yan et al., 2016) in the Amdo microterrane are interpreted as the arc associated with the northward subduction, which is missing in the central and western segments of the BNS and SQ due to burial or underthrusting during later tectonic events (Guynn et al., 2006). However,

the geodynamic divers for Middle-Late Jurassic record of the suture and its environs are hotly debated, and three models have previously been proposed: subduction initiation (Figure 1a; Tang, Zhai, Hu, Xiao, et al., 2018), Lhasa-Qiangtang collision (Figure 1d; Ma et al., 2017), and ridge subduction (Figure 1c; S.M. Li, Zhu, et al., 2016; Y.L. Li, He, et al., 2016). Both subduction initiation and Lhasa-Qiangtang collision are inconsistent with the key observations (see below). We favor ridge subduction and further develop it based on our new data from the Beila-Nagqu arc system (section 5.5.2).

Subduction initiation during 170–160 Ma (Figure 1a): The 170–160 Ma ophiolitic mafic rocks within the BNS also show SSZ signatures (Figures 10a–10c) and have been related to subduction initiation of the Bangong Tethys (Y.C. Zeng, Chen, et al., 2016; Tang, Zhai, Hu, Xiao, et al., 2018). This interpretation is challenged by the existence of the 190–180 Ma (Liu et al., 2016; B.D. Wang, Wang, et al., 2016) SSZ-type ophiolites (Figure 9) and a slightly older arc-trench system (194–170 Ma; section 4.3 and Figures 8a and 8b). Although these older rocks might possibly be explained as related to a separate branch of the Bangong Tethys, only a single arc-trench system during Middle-Late Jurassic (170–148 Ma) has been identified (Figure 8). Furthermore, subduction initiation should be associated with an overall extensional setting (Leitch, 1984; Stern et al., 2012; Stern & Bloomer, 1992), not the compressional environment documented for the Bangong Tethys (section 5.4).

Lhasa-Qiangtang collision at approximately 166 Ma (Figure 1d): Angular unconformities (166–160 Ma; Li, Guilmette, et al., 2017; Ma et al., 2017; A. Ma, Hu, et al., 2018; Sun et al., 2018) are invoked as evidence in support of this model. Such a scenario could also account for the magmatism from 160 to 148 Ma (Figures 9 and 10d–10f) as a result of slab break-off following the collision as well as the subsequent magmatic gap (148–125 Ma; Figure 9) reflecting a postcollisional environment. However, it is inconsistent with the existence of coeval (170–160 Ma; Figures 10a–10c; Tang, Zhai, Hu, Xiao, et al., 2018) and younger (approximately 148 Ma; Zhong, Liu, et al., 2017) SSZ-type ophiolites along the BNS (Figure 9), which are generally related to subduction rather than continent collisional processes (Dilek & Furnes, 2014). Besides, it requires an unrealistically high northward velocity of ~157 to ~625 mm/year for the Lhasa Terrane to collide with the Qiangtang Terrane. This is inferred by paleomagnetic results, which indicate that the difference in paleolatitude between the Lhasa and Qiangtang Terranes during 180–170 Ma is 20°–23° (Y. Ma, Yang, et al., 2018; Cao et al., 2019). In fact, the timing of Lhasa-Qiangtang collision has been investigated by a growing body of literature, and a favored time for collision of around 125–105 Ma has often been suggested (S.M. Li, Wang, et al., 2018; Zhu et al., 2016). Lines of evidence supporting this younger age for collision include (1) the active of within-plate magmatism (Figure 9) such as A-type granites (118–110 Ma; Wu et al., 2018; Fan et al., 2018) and OIB-type rocks (126–108 Ma; Fan et al., 2015; Zhu et al., 2016; Xu et al., 2017; Wu et al., 2019) within the BNS, and I-type felsic magmatism (Figure 9) in the SQ (125–105 Ma; J.X. Li, Qin, et al., 2014; Hao et al., 2016, 2018); (2) presence of detrital zircons of the SQ Jurassic arc in Duba formation from the Lhasa Terrane, which were deposited from 122 to 110 Ma (Lai et al., 2019); and (3) cessation of marine sedimentation during 125–118 Ma (Kapp et al., 2007). Therefore, Lhasa-Qiangtang collision likely occurred during 125–105 Ma and was not responsible for the Middle-Late Jurassic geological records.

5.5.2. Subparallel Ridge Subduction Model

The interaction between mid-ocean ridges and subduction zones is characterized by the development of triple junctions at the trench and slab windows beneath the arc-trench system, resulting in ophiolite generation and emplacement, uplift and deformation across the interaction site, slab window magmatism, and magmatic gaps (Bradley et al., 2003; Breitsprecher & Thorkelson, 2009; Delong & Fox, 1977; Georgieva et al., 2016; Gorring & Kay, 2001; Sisson et al., 2003). These signatures are similar to the geological records summarized above for the BNS and SQ. Orthogonal and subparallel ridge subduction represents the two end-members of interactions based on the arrangement of transform fault-ridge segments and the configuration between the transform-ridge system and trench (Figures 11 and S4; Thorkelson, 1996; Aragón et al., 2013). (1) During **orthogonal ridge subduction** (Figure 11a), only one triple junction develops and migrates, and a synchronous slab window forms between the two subducted slabs, for example, Southern America (Breitsprecher & Thorkelson, 2009). (2) **Subparallel ridge subduction** (Figure 11b) is characterized by the development of several coeval triple junctions along a convergent margin, for example, North America (Schellart et al., 2010), leading to a collision between subparallel ridge and trench. Subsequent, rather than synchronous, slab windows may develop after this collision by ridge subduction if it is not interrupted (e.g., Aragón et al., 2013) or by slab tearing caused by ridge-trench collision (e.g., Pallares

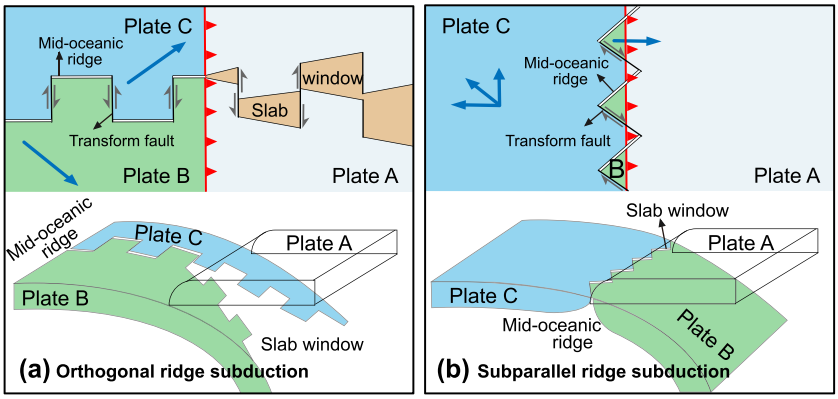

Figure 11. Schematic diagrams in plan view and 3-D block view showing two end-member models (orthogonal and subparallel) of ridge subduction based on the arrangement of transform fault-ridge segments and the configuration between transform-ridge system and trench (modified from Thorkelson, 1996). More models are illustrated in Figure S4 in the supporting information.

et al., 2007). For the Bangong Tethys case, we favor a subparallel ridge subduction model for the following reasons:

1. A compressional setting is expected across triple junctions (e.g., Bradley et al., 2003; Georgieva et al., 2016, 2019) due to the hot and buoyant nature of the mid-ridge oceanic lithosphere, which would result in coupling with the overriding plate. SSZ-type ophiolites could be generated at triple junctions as indicated by the modern example of the Taitao ophiolites at the Chile Triple Junction (Bourgois et al., 2016) and ancient examples in Alaska (61–50 Ma; Bradley et al., 2003) and northeast margin of Asia (56–46 Ma; Wu & Wu, 2019). The development of a compressional setting with coeval SSZ-type ophiolites (170–160 Ma) along strike of the BNS requires several coeval triple junctions along the trench. This is supported by paleogeography results, which suggest that the ridge-transform system of the Bangong Tethys was E-W trending and subparallel to the convergent margin (Figure 12a; Metcalfe, 2013; Gibbons et al., 2015).
2. The Middle-Late Jurassic igneous rocks (Figures 7 and 10d–10f) can be divided into two distinct E-W belts (Figure 9), including rock associations of slab-derived medium-K adakites and OIB-type rocks in

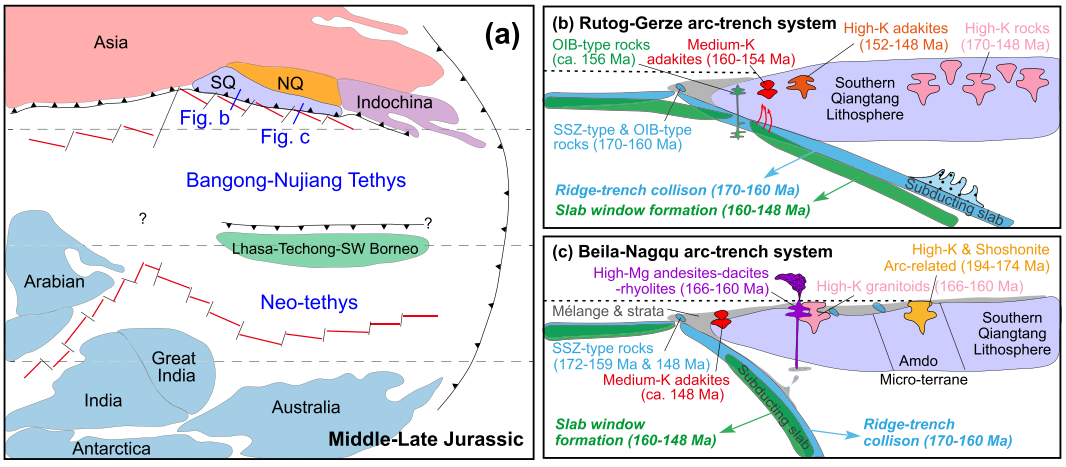

Figure 12. (a) Cartoon of plate reconstructions during Middle-Late Jurassic showing transform faults (black), mid-ridges (red), and subduction zones (triangles; modified from Gibbons et al., 2015; Metcalfe, 2013; Zhu et al., 2013). The transform-ridge system of Bangong Tethys is subparallel to the convergent margin of the southern Qiangtang subterrane. (b and c) Illustrations of the long-term evolution of ridge-subduction zone interaction in the western and eastern segments of the arc-trench system, respectively, involving ridge-trench parallel collision (170–160 Ma), slab window formation (160–148 Ma), and subduction termination (148–125 Ma; not shown).

the southern belt (160–148 Ma; S.M. Li, Zhu, et al., 2016; Y.L. Li, He, et al., 2016; Fan et al., 2016), and lower crust-derived high-K adakites (153–148 Ma; Hao et al., 2016), high-K intermediate-felsic intrusive rocks (170–148 Ma; J.X. Li, Qin, et al., 2014), and high-K high-Mg volcanic rocks (166–160 Ma; this study) in the northern belt. These two distinct magmatic belts define small slab windows beneath forearc regions and a normal subduction zone beneath the SQ (Figures 12b and 12c; S.M. Li, Zhu, et al., 2016), which is consistent with the geometry of subparallel ridge subduction.

3. During parallel ridge-trench interaction, subduction would likely be interrupted by the detachment of the subducted slab and coupling of the divergent ocean-floor slab to the former convergent margin through transform faults (Aragón et al., 2013). An example is in the western North American continent (Schellart et al., 2010), where the San Andreas fault system develops along the former subduction zone (Atwater & Stock, 1998). Such a scenario could account for the magmatic gap (148–125 Ma) and reactivation of magmatism (125–105 Ma) documented for the Bangong Tethyan case, which are related to subduction termination and final Lhasa-Qiangtang amalgamation, respectively. A similar example is suggested in the northeast Asian margin by a magmatic gap (56–46 Ma; Wu & Wu, 2019), which is interpreted as a result of the Izanagi-Pacific ridge parallel subduction.

Under the framework of subparallel ridge subduction (Figure 12), the following sequence of events is recognized. The compressional geodynamic environment as well as ophiolites were generated during ridge-trench encounter and collision (170–160 Ma). Then slab windows formed beneath the forearc and a normal subducting slab existed beneath the arc (160–148 Ma), producing two distinct magmatic belts. Subsequently, subduction termination resulted in the magmatic gap (148–125 Ma). Finally, slab detachment related to Lhasa-Qiangtang collision triggered the extensive Early Cretaceous magmatism (125–105 Ma).

6. Conclusions

1. A magmatic arc characterized by high-K calc-alkaline granitoids and high-Mg andesites, dacites, and rhyolites was active at 166–160 Ma around Daru Tso in the eastern Bangong-Nujiang suture.
2. The Beila-Nagqu mélange belt and the Daoban formation, to the south and north of the 166–160 Ma arc, formed contemporaneously and were sourced from the arc.
3. Our new data in the eastern segment, along with existing data in the western segment of the suture, imply the development of an overall compressional convergent margin extending over 1,200 km along strike during Middle-Late Jurassic.
4. A subparallel ridge-subduction zone interaction event provides a viable model to explain the diverse geological records of the BNS and Qiangtang Terrane and involves subparallel ridge-trench collision (170–160 Ma), slab window formation (160–148 Ma), and subsequent subduction termination (148–125 Ma).

Acknowledgments
The data supporting this paper can be accessed from the supporting information and Open Science Framework (https://osf.io/pvg68/). We are grateful to John Geissman (Editor), Yener Eyuboglu, and an anonymous reviewer for their constructive reviews. This research was financially co-supported by the MOST of China (2016YFC0600407 and 2016YFC0600304); the Second Tibetan Plateau Scientific Expedition and Research Program (STEP; 2019QZKK0702); the Chinese National Natural Science Foundation (grants 91755207, 41872060, and 41902047); the Programme of Introducing Talents of Discipline to Universities (i.e., the 111 project; B18048); the Australian Research Council (grant FL160100168); the MOST Special Fund from the State Key Laboratory of Geological Processes and Mineral Resources, China University of Geosciences (grant MSFGPMR201802); and China Postdoctoral Science Foundation (grant 2018M640162). This is UTD Geosciences contribution 1354. This is CUGB petrogeochemical contribution PGC2015-0040.

References

Andersen, T. (2002). Correction of common lead in U-Pb analyses that do not report Pb-204. *Chemical Geology*, *192*(1-2), 59–79. https://doi.org/10.1016/s0009-2541(02)00195-x

Aragón, E., Pinotti, L., D'Eramo, F., Castro, A., Rabbia, O., Coniglio, J., et al. (2013). The Farallon-Aluk ridge collision with South America: Implications for the geochemical changes of slab window magmas from fore- to back-arc. *Geoscience Frontiers*, *4*(4), 377–388. https://doi.org/10.1016/j.gsf.2012.12.004

Atwater, T., & Stock, J. (1998). Pacific-North America plate tectonics of the Neogene southwestern United States: An update. *International Geology Review*, *40*(5), 375–402. https://doi.org/10.1080/00206819809465216

Bourgois, J., Lagabrielle, Y., Martin, H., Dyment, J., Frutos, J., Cisternas, M. E. J. P., & Geophysics, A. (2016). A review on forearc ophiolite obduction, adakite-like generation, and slab window development at the Chile Triple Junction area: Uniformitarian framework for spreading-ridge subduction. *Pure and Applied Geophysics*, *173*(10-11), 3217–3246. https://doi.org/10.1007/s00024-016-1317-9

Brach-Papa, C., Van Bocxstaele, M., Ponzevera, E., & Quétel, C. R. (2009). Fit for purpose validated method for the determination of the strontium isotopic signature in mineral water samples by multi-collector inductively coupled plasma mass spectrometry. *Spectrochimica Acta Part B: Atomic Spectroscopy*, *64*(3), 229–234. https://doi.org/10.1016/j.sab.2009.01.012

Bradley, D. C., Kusky, T. M., Haeussler, P. J., Goldfarb, R. J., Miller, M. L., Dumoulin, J. A., et al. (2003). Geologic signature of early Tertiary ridge subduction in Alaska. *Geological Society of America Special Papers*, *371*, 19–49. https://doi.org/10.1130/0-8137-2371-X.19

Breitsprecher, K., & Thorkelson, D. J. (2009). Neogene kinematic history of Nazca–Antarctic–Phoenix slab windows beneath Patagonia and the Antarctic Peninsula. *Tectonophysics*, *464*(1–4), 10–20. https://doi.org/10.1016/j.tecto.2008.02.013

Cai, F., Ding, L., Laskowski, A. K., Kapp, P., Wang, H., Xu, Q., & Zhang, L. (2016). Late Triassic paleogeographic reconstruction along the Neo–Tethyan Ocean margins, southern Tibet. *Earth and Planetary Science Letters*, *435*, 105–114. https://doi.org/10.1016/j.epsl.2015.12.027

Cao, Y., Sun, Z., Li, H., Pei, J., Liu, D., Zhang, L., et al. (2019). New paleomagnetic results from Middle Jurassic limestones of the Qiangtang Terrane, Tibet: Constraints on the evolution of the Bangong-Nujiang Ocean. *Tectonics*, *38*(1), 215–232. https://doi.org/10.1029/2017TC004842

Castro, A. (2019). The dual origin of I-type granites: The contribution from experiments. *Geological Society, London, Special Publications*, *491*, SP491-2018-2110. https://doi.org/10.1144/sp491-2018-110

Castro, A., Gerya, T., Garcia-Casco, A., Fernandez, C., Diaz-Alvarado, J., Moreno-Ventas, I., & Low, I. (2010). Melting relations of MORB-sediment melanges in underplated mantle wedge plumes: Implications for the origin of Cordilleran-type batholiths. *Journal of Petrology*, *51*(6), 1267–1295. https://doi.org/10.1093/petrology/egq019

Castro, A., & Gerya, T. V. (2008). Magmatic implications of mantle wedge plumes: Experimental study. *Lithos*, *103*(1), 138–148. https://doi.org/10.1016/j.lithos.2007.09.012

Cawood, P. A., Kröner, A., Collins, W. J., Kusky, T. M., Mooney, W. D., & Windley, B. F. (2009). Accretionary orogens through Earth history. *Geological Society, London, Special Publications*, *318*(1), 1–36. https://doi.org/10.1144/sp318.1

Chappell, B. W. (1999). Aluminium saturation in I- and S-type granites and the characterization of fractionated haplogranites. *Lithos*, *46*(3), 535–551. https://doi.org/10.1016/S0024-4937(98)00086-3

Chappell, B. W., & White, A. J. R. (2001). Two contrasting granite types: 25 years later. *Australian Journal of Earth Sciences*, *48*(4), 489–499. https://doi.org/10.1046/j.1440-0952.2001.00882.x

Cheng, J., & Xu, G. (1987). Geologic map of the Ritu region with report, 598 pp (in Chinese with English abstract), Tibetan Bureau of Geological and Mineral Resources, Chengdu, People's Republic of China.

Codillo, E. A., Le Roux, V., & Marschall, H. R. (2018). Arc-like magmas generated by mélange-peridotite interaction in the mantle wedge. *Nature Communications*, *9*(1), 2864. https://doi.org/10.1038/s41467-018-05313-2

Delong, S. E., & Fox, P. J. (1977). Geological consequences of ridge subduction. In M. Talwani & W. C. Pittman, III (Eds.), *Island arcs, deep sea trenches and back-arc basins* (pp. 221–228). Washington, DC: American Geophysical Union. https://doi.org/10.1029/ME001p0221

Dewey, J., & Spall, H. (1975). Pre-Mesozoic plate tectonics: How far back in Earth history can the Wilson Cycle be extended? *Geology*, *3*(8), 422–424. https://doi.org/10.1130/0091-7613(1975)3<422:Ppthfb>2.0.Co;2

Dickinson, W. R., & Gehrels, G. E. (2009). Use of U–Pb ages of detrital zircons to infer maximum depositional ages of strata: A test against a Colorado Plateau Mesozoic database. *Earth and Planetary Science Letters*, *288*(1), 115–125. https://doi.org/10.1016/j.epsl.2009.09.013

Dilek, Y., & Furnes, H. (2014). Ophiolites and their origins. *Elements*, *10*(2), 93–100. https://doi.org/10.2113/gselements.10.2.93

Dong, C., Li, C., Wan, Y., Wang, W., Wu, Y., Xie, H., & Liu, D. (2011). Detrital zircon age model of Ordovician Wenquan quartzite south of Lungmuco-Shuanghu Suture in the Qiangtang area, Tibet: Constraint on tectonic affinity and source regions. *Science China Earth Sciences*, *54*(7), 1034–1042. https://doi.org/10.1007/s11430-010-4166-x

Dong, X., Zhang, Z., & Santosh, M. (2010). Zircon U-Pb chronology of the Nyingtri Group, Southern Lhasa Terrane, Tibetan Plateau: Implications for Grenvillian and Pan-African provenance and Mesozoic-Cenozoic metamorphism. *The Journal of Geology*, *118*(6), 677–690. https://doi.org/10.1086/656355

Errázuriz-Henao, C., Gómez-Tuena, A., Duque-Trujillo, J., & Weber, M. (2019). The role of subducted sediments in the formation of intermediate mantle-derived magmas from the Northern Colombian Andes. *Lithos*, *336-337*, 151–168. https://doi.org/10.1016/j.lithos.2019.04.007

Fan, J.-J., Li, C., Sun, Z.-M., Xu, W., Wang, M., & Xie, C.-M. (2018). Early Cretaceous MORB-type basalt and A-type rhyolite in northern Tibet: Evidence for ridge subduction in the Bangong–Nujiang Tethyan Ocean. *Journal of Asian Earth Sciences*, *154*, 187–201. https://doi.org/10.1016/j.jseaes.2017.12.020

Fan, J.-J., Li, C., Wu, H., Zhang, T.-Y., Wang, M., Chen, J.-W., & Xu, J.-X. (2016). Late Jurassic adakitic granodiorite in the Dong Co area, northern Tibet: Implications for subduction of the Bangong–Nujiang oceanic lithosphere and related accretion of the Southern Qiangtang terrane. *Tectonophysics*. https://doi.org/10.1016/j.tecto.2016.10.026

Fan, J.-J., Li, C., Xie, C.-M., Wang, M., & Chen, J.-W. (2015). The evolution of the Bangong–Nujiang Neo-Tethys Ocean: Evidence from zircon U–Pb and Lu–Hf isotopic analyses of Early Cretaceous oceanic islands and ophiolites. *Tectonophysics*, *655*, 27–40. https://doi.org/10.1016/j.tecto.2015.04.019

Gaffney, A. M., Blichert-Toft, J., Nelson, B. K., Bizzarro, M., Rosing, M., & Albarède, F. (2007). Constraints on source-forming processes of West Greenland kimberlites inferred from Hf–Nd isotope systematics. *Geochimica et Cosmochimica Acta*, *71*(11), 2820–2836. https://doi.org/10.1016/j.gca.2007.03.009

Gehrels, G., Kapp, P., DeCelles, P., Pullen, A., Blakey, R., Weislogel, A., et al. (2011). Detrital zircon geochronology of pre-Tertiary strata in the Tibetan-Himalayan orogen. *Tectonics*, *30*, TC5016. https://doi.org/10.1029/2011TC002868

Georgieva, V., Gallagher, K., Sobczyk, A., Sobel, E. R., Schildgen, T. F., Ehlers, T. A., & Strecker, M. R. (2019). Effects of slab-window, alkaline volcanism, and glaciation on thermochronometer cooling histories, Patagonian Andes. *Earth and Planetary Science Letters*, *511*, 164–176. https://doi.org/10.1016/j.epsl.2019.01.030

Georgieva, V., Melnick, D., Schildgen, T. F., Ehlers, T. A., Lagabrielle, Y., Enkelmann, E., & Strecker, M. R. (2016). Tectonic control on rock uplift, exhumation, and topography above an oceanic ridge collision: Southern Patagonian Andes (47°S), Chile. *Tectonics*, *35*(6), 1317–1341. https://doi.org/10.1002/2016tc004120

Gerya, T. V., & Yuen, D. A. (2003). Rayleigh–Taylor instabilities from hydration and melting propel "cold plumes" at subduction zones. *Earth and Planetary Science Letters*, *212*(1), 47–62. https://doi.org/10.1016/S0012-821X(03)00265-6

Gibbons, A. D., Zahirovic, S., Müller, R. D., Whittaker, J. M., & Yatheesh, V. (2015). A tectonic model reconciling evidence for the collisions between India, Eurasia and intra-oceanic arcs of the central-eastern Tethys. *Gondwana Research*, *28*(2), 451–492. https://doi.org/10.1016/j.gr.2015.01.001

Gorring, M. L., & Kay, S. M. (2001). Mantle processes and sources of Neogene slab window magmas from southern Patagonia, Argentina. *Journal of Petrology*, *42*(6), 1067–1094. https://doi.org/10.1093/petrology/42.6.1067

Guo, L., Zhang, H.-F., Harris, N., Xu, W.-C., & Pan, F.-B. (2016). Late Devonian-Early Carboniferous magmatism in the Lhasa terrane and its tectonic implications: Evidences from detrital zircons in the Nyingchi Complex. *Lithos*, *245*, 47–59. https://doi.org/10.1016/j.lithos.2015.06.018

Guo, L., Zhang, H.-F., Harris, N., Xu, W.-C., & Pan, F.-B. (2017). Detrital zircon U–Pb geochronology, trace-element and Hf isotope geochemistry of the metasedimentary rocks in the Eastern Himalayan syntaxis: Tectonic and paleogeographic implications. *Gondwana Research*, *41*, 207–221. https://doi.org/10.1016/j.gr.2015.07.013

Guynn, J., Kapp, P., Gehrels, G. E., & Ding, L. (2012). U–Pb geochronology of basement rocks in central Tibet and paleogeographic implications. *Journal of Asian Earth Sciences*, *43*(1), 23–50. https://doi.org/10.1016/j.jseaes.2011.09.003

Guynn, J. H., Kapp, P., Pullen, A., Heizler, M., Gehrels, G., & Ding, L. (2006). Tibetan basement rocks near Amdo reveal "missing" Mesozoic tectonism along the Bangong suture, central Tibet. *Geology*, *34*(6), 505–508. https://doi.org/10.1130/g22453.1

Hao, L.-L., Wang, Q., Wyman, D. A., Ou, Q., Dan, W., Jiang, Z.-Q., et al. (2016). Underplating of basaltic magmas and crustal growth in a continental arc: Evidence from Late Mesozoic intermediate–felsic intrusive rocks in southern Qiangtang, central Tibet. *Lithos*, *245*, 223–242. https://doi.org/10.1016/j.lithos.2015.09.015

Hao, L.-L., Wang, Q., Zhang, C., Ou, Q., Yang, J.-H., Dan, W., & Jiang, Z.-Q. (2018). Oceanic plateau subduction during closure of the Bangong-Nujiang Tethyan Ocean: Insights from central Tibetan volcanic rocks. *GSA Bulletin*. https://doi.org/10.1130/B32045.1

Hastie, A. R., Kerr, A. C., Pearce, J. A., & Mitchell, S. F. (2007). Classification of altered volcanic island arc rocks using immobile trace elements: Development of the Th–Co discrimination diagram. *Journal of Petrology*, *48*(12), 2341–2357. https://doi.org/10.1093/petrology/egm062

Hu, P.-Y., Zhai, Q.-G., Jahn, B.-M., Wang, J., Li, C., Chung, S.-L., et al. (2017). Late Early Cretaceous magmatic rocks (118–113 Ma) in the middle segment of the Bangong–Nujiang suture zone, Tibetan Plateau: Evidence of lithospheric delamination. *Gondwana Research*, *44*, 116–138. https://doi.org/10.1016/j.gr.2016.12.005

Hu, X., Garzanti, E., Wang, J., Huang, W., An, W., & Webb, A. (2016). The timing of India-Asia collision onset: Facts, theories, controversies. *Earth-Science Reviews*, *160*, 264–299. https://doi.org/10.1016/j.earscirev.2016.07.014

Huang, Q., Li, J., Cai, Z., Xia, L., Yuan, Y., Liu, H., & Xia, B. (2015). Geochemistry, geochronology, Sr-Nd isotopic compositions of Jiang Tso ophiolite in the middle segment of the Bangong-Nujiang suture zone and their geological significance. *Acta Geologica Sinica - English Edition*, *89*(2), 389–401. https://doi.org/10.1111/1755-6724.12437

Huang, Q.-T., Liu, W.-L., Xia, B., Cai, Z.-R., Chen, W.-Y., Li, J.-F., & Yin, Z.-X. (2017). Petrogenesis of the Majiari ophiolite (western Tibet, China): Implications for intra-oceanic subduction in the Bangong–Nujiang Tethys. *Journal of Asian Earth Sciences*, *146*, 337–351. https://doi.org/10.1016/j.jseaes.2017.06.008

Huang, T.-T., Xu, J.-F., Chen, J.-L., Wu, J.-B., & Zeng, Y.-C. (2016). Sedimentary record of Jurassic northward subduction of the Bangong–Nujiang Ocean: Insights from detrital zircons. *International Geology Review*, *1-19*. https://doi.org/10.1080/00206814.2016.1218801

Ishizuka, O., Tani, K., & Reagan, M. K. (2014). Izu-Bonin-Mariana forearc crust as a modern ophiolite analogue. *Elements*, *10*(2), 115–120. https://doi.org/10.2113/gselements.10.2.115

Kapp, P., & DeCelles, P. G. (2019). Mesozoic–Cenozoic geological evolution of the Himalayan-Tibetan orogen and working tectonic hypotheses. *American Journal of Science*, *319*(3), 159–254. https://doi.org/10.2475/03.2019.01

Kapp, P., DeCelles, P. G., Gehrels, G. E., Heizler, M., & Ding, L. (2007). Geological records of the Lhasa-Qiangtang and Indo-Asian collisions in the Nima area of central Tibet. *Geological Society of America Bulletin*, *119*(7-8), 917–933. https://doi.org/10.1130/b26033.1

Kapp, P., Murphy, M. A., Yin, A., Harrison, T. M., Ding, L., & Guo, J. H. (2003). Mesozoic and Cenozoic tectonic evolution of the Shiquanhe area of western Tibet. *Tectonics*, *22*(4), 1029. https://doi.org/10.1029/2001TC001332

Kapp, P., Yin, A., Harrison, T. M., & Ding, L. (2005). Cretaceous-Tertiary shortening, basin development, and volcanism in central Tibet. *Geological Society of America Bulletin*, *117*(7-8), 865–878. https://doi.org/10.1130/1325595.1

Kemp, A. I. S., Hawkesworth, C. J., Foster, G. L., Paterson, B. A., Woodhead, J. D., Hergt, J. M., et al. (2007). Magmatic and crustal differentiation history of granitic rocks from Hf-O isotopes in zircon. *Science*, *315*(5814), 980–983. https://doi.org/10.1126/science.1136154

Kong, W., Jiang, Z., Zhang, X., Xu, X., Fang, M., Feng, J., & Xiao, X. (2017). U-Pb ages and tectonic significance of SSZ ophiolite zircon in Baingoin County, Tibet (in Chinese with English abstract). *Resources Environment & Engineering*, *31*(6), 669–674.

Lai, W., Hu, X., Garzanti, E., Xu, Y., Ma, A., & Li, W. (2019). Early Cretaceous sedimentary evolution of the northern Lhasa terrane and the timing of initial Lhasa-Qiangtang collision. *Gondwana Research*, *73*, 136–152. https://doi.org/10.1016/j.gr.2019.03.016

Le Maitre, R. W. (2002). *Igneous rocks: A classification and glossary of terms: Recommendations of international union of geological sciences subcommission on the systematics of igneous rocks* (p. 236). Cambridge: Cambridge University Press. https://doi.org/10.1017/CBO9780511535581

Lee, C.-T. A., Morton, D. M., Kistler, R. W., & Baird, A. K. (2007). Petrology and tectonics of Phanerozoic continent formation: From island arcs to accretion and continental arc magmatism. *Earth and Planetary Science Letters*, *263*(3), 370–387. https://doi.org/10.1016/j.epsl.2007.09.025

Leitch, E. C. (1984). Island arc elements and arc-related ophiolites. *Tectonophysics*, *106*(3), 177–203. https://doi.org/10.1016/0040-1951(84)90176-8

Li, C., Li, Z., Cao, H., & Zeng, M. (2018). Newly discovered ca. 163 Ma OIB-type diabase dike from the Shiquanhe ophiolites, western Tibet (in Chinese with English abstract). *Acta Geologica Sinica*, *92*(6), 2443–2444.

Li, G., Sandiford, M., Liu, X., Xu, Z., Wei, L., & Li, H. (2014). Provenance of Late Triassic sediments in central Lhasa terrane, Tibet and its implication. *Gondwana Research*, *25*(4), 1680–1689. https://doi.org/10.1016/j.gr.2013.06.019

Li, H. F., Liu, Z., Chen, W., Wang, N., Wang, J., Zhang, K., et al. (2019). The discovery of high-Mg rhyolitic rocks in Peng Tso area, Tibet and its significance for evolution of Bangong-Nujiang Ocean (in Chinese with English abstract). *Acta Petrologica Sinica*, *35*(3), 799–815.

Li, J., Xia, B., Xia, L., Xu, L., Liu, W., Cai, Z., & Yang, Z. (2013). Geochronology of the Dong Tso ophiolite and the tectonic environment. *Acta Geologica Sinica - English Edition*, *87*(6), 1604–1616. https://doi.org/10.1111/1755-6724.12162

Li, J.-X., Qin, K.-Z., Li, G.-M., Richards, J. P., Zhao, J.-X., & Cao, M.-J. (2014). Geochronology, geochemistry, and zircon Hf isotopic compositions of Mesozoic intermediate–felsic intrusions in central Tibet: Petrogenetic and tectonic implications. *Lithos*, *198–199*, 77–91. https://doi.org/10.1016/j.lithos.2014.03.025

Li, L., Fan, M., Garzione, C. N., Li, X., & Li, X. (2019). Jurassic sedimentation in the south-central Qiangtang terrane reveals successive terrane collisions in central Tibet. *Geosphere*. https://doi.org/10.1130/ges01649.1

Li, S., Ding, L., Guilmette, C., Fu, J., Xu, Q., Yue, Y., & Henrique-Pinto, R. (2017). The subduction-accretion history of the Bangong-Nujiang Ocean: Constraints from provenance and geochronology of the Mesozoic strata near Gaize, central Tibet. *Tectonophysics*, *702*, 42–60. https://doi.org/10.1016/j.tecto.2017.02.023

Li, S., Guilmette, C., Ding, L., Xu, Q., Fu, J.-J., & Yue, Y.-H. (2017). Provenance of Mesozoic clastic rocks within the Bangong-Nujiang suture zone, central Tibet: Implications for the age of the initial Lhasa-Qiangtang collision. *Journal of Asian Earth Sciences*, *147*(Supplement C), 469–484. https://doi.org/10.1016/j.jseaes.2017.08.019

Li, S.-M., Wang, Q., Zhu, D.-C., Stern, R. J., Cawood, P. A., Sui, Q.-L., & Zhao, Z. (2018). One or two Early Cretaceous arc systems in the Lhasa Terrane, southern Tibet. *Journal of Geophysical Research - Solid Earth*, *123*(5), 3391–3413. https://doi.org/10.1002/2018JB015582

Li, S. M., Zhu, D. C., Wang, Q., Zhao, Z., Zhang, L. L., Liu, S. A., et al. (2016). Slab-derived adakites and subslab asthenosphere-derived OIB-type rocks at 156 ± 2 Ma from the north of Gerze, central Tibet: Records of the Bangong–Nujiang oceanic ridge subduction during the Late Jurassic. *Lithos*, *262*, 456–469. https://doi.org/10.1016/j.lithos.2016.07.029

Li, S. M., Zhu, D. C., Wang, Q., Zhao, Z. D., Sui, Q. L., Liu, S. A., et al. (2014). Northward subduction of Bangong–Nujiang Tethys: Insight from Late Jurassic intrusive rocks from Bangong Tso in western Tibet. *Lithos*, *205*, 284–297. https://doi.org/10.1016/j.lithos.2014.07.010

Li, X., Wang, B., Liu, H., Wang, L., & Chen, L. (2015). The Late Jurassic high-Mg andesites in the Daru Tso area, Tibet: Evidence for the subduction of the Bangong Co–Nujiang River oceanic lithosphere (in Chinese with English abstract). *Geological Bulletin of China*, *34*(2/3), 251–261.

Li, Y. L., He, J., Han, Z., Wang, C., Ma, P., Zhou, A., et al. (2016). Late Jurassic sodium-rich adakitic intrusive rocks in the southern Qiangtang terrane, central Tibet, and their implications for the Bangong–Nujiang Ocean subduction. *Lithos*, *245*, 34–46. https://doi.org/10.1016/j.lithos.2015.10.014

Liu, M. (2012). Petrogenesis and Tectonic significance of early Jurassic alkalic Pluton in Nyainrong microcontinent, central Tibet (in Chinese with English abstract). Doctoral thesis, China University of Geosciences.

Liu, T., Zhai, Q.-G., Wang, J., Bao, P.-S., Qiangba, Z., Tang, S.-H., & Tang, Y. (2016). Tectonic significance of the Dongqiao ophiolite in the north-central Tibetan Plateau: Evidence from zircon dating, petrological, geochemical and Sr–Nd–Hf isotopic characterization. *Journal of Asian Earth Sciences*, *116*, 139–154. https://doi.org/10.1016/j.jseaes.2015.11.014

Liu, W.-L., Xia, B., Zhong, Y., Cai, J.-X., Li, J.-F., Liu, H.-F., et al. (2014). Age and composition of the Rebang Co and Julu ophiolites, central Tibet: Implications for the evolution of the Bangong Meso-Tethys. *International Geology Review*, *56*(4), 430–447. https://doi.org/10.1080/00206814.2013.873356

Liu, Y., Gao, S., Kelemen, P. B., & Xu, W. (2008). Recycled crust controls contrasting source compositions of Mesozoic and Cenozoic basalts in the North China Craton. *Geochimica et Cosmochimica Acta*, *72*(9), 2349–2376. https://doi.org/10.1016/j.gca.2008.02.018

Liu, Y. S., Gao, S., Hu, Z. C., Gao, C. G., Zong, K. Q., & Wang, D. B. (2010). Continental and oceanic crust recycling-induced melt–peridotite interactions in the trans-north China orogen: U–Pb dating, Hf isotopes and trace elements in zircons from mantle xenoliths. *Journal of Petrology*, *51*(1-2), 537–571. https://doi.org/10.1093/petrology/egp082

Ludwig, K. R. (2003). *User's manual for Isoplot 3.00: A geochronological toolkit for Microsoft Excel*, Berkeley Geochronology Centre Special Publication. Kenneth R. Ludwig.

Ma, A., Hu, X., Garzanti, E., Han, Z., & Lai, W. (2017). Sedimentary and tectonic evolution of the southern Qiangtang basin: Implications for the Lhasa-Qiangtang collision timing. *Journal of Geophysical Research - Solid Earth*, *122*(7), 4790–4813. https://doi.org/10.1002/2017JB014211

Ma, A., Hu, X., Kapp, P., Han, Z., Lai, W., & BouDagher-Fadel, M. (2018). The disappearance of a Late Jurassic remnant sea in the southern Qiangtang Block (Shamuluo formation, Najiangco area): Implications for the tectonic uplift of central Tibet. *Palaeogeography, Palaeoclimatology, Palaeoecology*, *506*, 30–47. https://doi.org/10.1016/j.palaeo.2018.06.005

Ma, Y., Yang, T., Bian, W., Jin, J., Wang, Q., Zhang, S., et al. (2018). A stable southern margin of Asia during the Cretaceous: Paleomagnetic constraints on the Lhasa-Qiangtang collision and the maximum width of the Neo-Tethys. *Tectonics*, *37*(10), 3853–3876. https://doi.org/10.1029/2018TC005143

Marschall, H. R., & Schumacher, J. C. (2012). Arc magmas sourced from mélange diapirs in subduction zones. *Nature Geoscience*, *5*, 862. https://doi.org/10.1038/ngeo1634

Martinod, J., Husson, L., Roperch, P., Guillaume, B., & Espurt, N. (2010). Horizontal subduction zones, convergence velocity and the building of the Andes. *Earth and Planetary Science Letters*, *299*(3), 299–309. https://doi.org/10.1016/j.epsl.2010.09.010

McCarron, J., & Smellie, J. (1998). Tectonic implications of fore-arc magmatism and generation of high-magnesian andesites: Alexander Island, Antarctica. *Journal of the Geological Society*, *155*(2), 269–280. https://doi.org/10.1144/gsjgs.155.2.0269

Metcalfe, I. (2013). Gondwana dispersion and Asian accretion: Tectonic and palaeogeographic evolution of eastern Tethys. *Journal of Asian Earth Sciences*, *66*, 1–33. https://doi.org/10.1016/j.jseaes.2012.12.020

Miyashiro, A. (1974). Volcanic rock series in island arcs and active continentalmargins. *American Journal of Science*, *274*, 321–355.

Murphy, J. B., & Nance, R. D. (1991). Supercontinent model for the contrasting character of Late Proterozoic orogenic belts. *Geology*, *19*(5), 469–472. https://doi.org/10.1130/0091-7613(1991)019<0469:Smftcc>2.3.Co;2

Nielsen, S. G., & Marschall, H. R. (2017). Geochemical evidence for mélange melting in global arcs. *Science Advances*, *3*(4), e1602402. https://doi.org/10.1126/sciadv.1602402

Pallares, C., Maury, R. C., Bellon, H., Royer, J.-Y., Calmus, T., Aguillón-Robles, A., et al. (2007). Slab-tearing following ridge-trench collision: Evidence from Miocene volcanism in Baja California, México. *Journal of Volcanology and Geothermal Research*, *161*(1), 95–117. https://doi.org/10.1016/j.jvolgeores.2006.11.002

Pan, G. T., Ding, J., Yao, D. S., & Wang, L. Q. (2004). *Guidebook of 1:1,500,000 geologic map of the Qinghai–Xizang (Tibet) plateau and adjacent areas 1–148 (in Chinese with English abstract)*. Chengdu, China: Cartographic Publishing House.

Parolari, M., Gómez-Tuena, A., Guadalupe, J., Cavazos-Tovar, J., & Hernández-Quevedo, G. (2018). A balancing act of crust creation and destruction along the western Mexican convergent margin. *Geology*, *46*(5), 455–458. https://doi.org/10.1130/G39972.1

Pearce, J. A. (2014). Immobile element fingerprinting of ophiolites. *Elements*, *10*(2), 101–108. https://doi.org/10.2113/gselements.10.2.101

Pullen, A., Kapp, P., Gehrels, G. E., Ding, L., & Zhang, Q. (2011). Metamorphic rocks in central Tibet: Lateral variations and implications for crustal structure. *Geological Society of America Bulletin*, *123*(3-4), 585–600. https://doi.org/10.1130/b30154.1

Pullen, A., Kapp, P., Gehrels, G. E., Vervoort, J. D., & Ding, L. (2008). Triassic continental subduction in central Tibet and Mediterranean-style closure of the Paleo-Tethys Ocean. *Geology*, *36*(5), 351–354. https://doi.org/10.1130/g24435a.1

Rapp, R., Shimizu, N., Norman, M., & Applegate, G. (1999). Reaction between slab-derived melts and peridotite in the mantle wedge: Experimental constraints at 3.8 GPa. *Chemical Geology*, *160*(4), 335–356. https://doi.org/10.1016/S0009-2541(99)00106-0

Reagan, M. K., Heaton, D. E., Schmitz, M. D., Pearce, J. A., Shervais, J. W., & Koppers, A. A. P. (2019). Forearc ages reveal extensive short-lived and rapid seafloor spreading following subduction initiation. *Earth and Planetary Science Letters*, *506*, 520–529. https://doi.org/10.1016/j.epsl.2018.11.020

Schellart, W. P., Stegman, D. R., Farrington, R. J., Freeman, J., & Moresi, L. (2010). Cenozoic tectonics of western North America controlled by evolving width of Farallon slab. *Science*, *329*(5989), 316–319. https://doi.org/10.1126/science.1190366

Shi, R., Yang, J., Xu, Z., & Qi, X. (2008). The Bangong Lake ophiolite (NW Tibet) and its bearing on the tectonic evolution of the Bangong–Nujiang suture zone. *Journal of Asian Earth Sciences*, *32*(5-6), 438–457. https://doi.org/10.1016/j.jseaes.2007.11.011

Shi, R. D. (2007). SHRIMP dating of the Bangong Lake SSZ-type ophiolite: Constraints on the closure time of ocean in the Bangong Lake-Nujiang River, northwestern Tibet. *Chinese Science Bulletin*, *52*(7), 936–941. https://doi.org/10.1007/s11434-007-0134-z

Sisson, V. B., Pavlis, T. L., Roeske, S. M., & Thorkelson, D. J. (2003). Introduction: An overview of ridge-trench interactions in modern and ancient settings. *Geological Society of America Special Papers*, *1-18*.

Stern, R. J. (2002). Subduction zones. *Reviews of Geophysics*, *40*(4), 1012. https://doi.org/10.1029/2001RG000108

Stern, R. J., & Bloomer, S. H. (1992). Subduction zone infancy: Examples from the Eocene Izu-Bonin-Mariana and Jurassic California arcs. *Geological Society of America Bulletin*, *104*(12), 1621–1636. https://doi.org/10.1130/0016-7606(1992)104<1621:Szieft>2.3.Co;2

Stern, R. J., & Gerya, T. (2018). Subduction initiation in nature and models: A review. *Tectonophysics*, *746*, 173–198. https://doi.org/10.1016/j.tecto.2017.10.014

Stern, R. J., Reagan, M., Ishizuka, O., Ohara, Y., & Whattam, S. (2012). To understand subduction initiation, study forearc crust: To understand forearc crust, study ophiolites. *Lithosphere*. https://doi.org/10.1130/l183.1

Sun, G., Hu, X., Xu, Y., & BouDagher-Fadel, M. K. (2018). Discovery of Middle Jurassic trench deposits in the Bangong-Nujiang suture zone: Implications for the timing of Lhasa-Qiangtang initial collision. *Tectonophysics*. https://doi.org/10.1016/j.tecto.2018.12.001

Sun, S.-S., & McDonough, W. F. (1989). Chemical and isotopic systematics of oceanic basalts: Implications for mantle composition and processes. *Geological Society, London, Special Publications*, *42*(1), 313–345. https://doi.org/10.1144/gsl.sp.1989.042.01.19

Tang, Y., Zhai, Q., Hu, P., Xiao, X., & Wang, H. (2018). Petrology, geochemistry and geochronology of the Zhongcang ophiolite, northern Tibet: Implications for the evolution of the Bangong-Nujiang Ocean. *Geoscience Frontiers*. https://doi.org/10.1016/j.gsf.2018.05.007

Tang, Y., Zhai, Q.-G., Hu, P.-Y., Wang, J., Xiao, X.-C., Wang, H.-T., et al. (2018). Rodingite from the Beila ophiolite in the Bangong–Nujiang suture zone, northern Tibet: New insights into the formation of ophiolite-related rodingite. *Lithos*, *316-317*, 33–47. https://doi.org/10.1016/j.lithos.2018.07.006

Tatsumi, Y. (2006). High-Mg andesites in the Setouchi volcanic belt, southwestern Japan: Analogy to Archean magmatism and continental crust formation? *Annual Review of Earth and Planetary Sciences*, *34*, 467–499. https://doi.org/10.1146/annurev.earth.34.031405.125014

Thorkelson, D. J. (1996). Subduction of diverging plates and the principles of slab window formation. *Tectonophysics*, *255*(1–2), 47–63. https://doi.org/10.1016/0040-1951(95)00106-9

Wang, B. D., Wang, L. Q., Chung, S. L., Chen, J. L., Yin, F. G., Liu, H., et al. (2016). Evolution of the Bangong–Nujiang Tethyan ocean: Insights from the geochronology and geochemistry of mafic rocks within ophiolites. *Lithos*, *245*, 18–33. https://doi.org/10.1016/j.lithos.2015.07.016

Wang, L. Q., Pan, G. T., Ding, J., & Yao, D. S. (2013). *Guidebook of 1:1,500,000 geological map of the Qinghai–Xizang (Tibet) Plateau and adjacent areas (in Chinese with English abstract)* (pp. 1–288). Beijing, China: Geological Publishing House.

Wang, M., Li, C., & Xie, C. M. (2016). Dating of detrital zircons from the Dabure clastic rocks: The discovery of Neoproterozoic strata in southern Qiangtang, Tibet. *International Geology Review*, *58*(2), 216–227. https://doi.org/10.1080/00206814.2015.1065207

Wang, M., Peng, S.-Y., Li, C., & Zhang, T.-Y. (2018). Palaeontology and U–Pb detrital zircon geochronology of Upper Triassic strata on the northern margin of the Bangong Co–Nujiang Suture Zone, Tibet: Constraints on the age of opening of the Meso-Tethys. *Journal of Asian Earth Sciences*. https://doi.org/10.1016/j.jseaes.2018.08.015

Wang, Q., Zhu, D.-C., Zhao, Z.-D., Liu, S.-A., Chung, S.-L., Li, S.-M., et al. (2014). Origin of the ca. 90 Ma magnesia-rich volcanic rocks in SE Nyima, central Tibet: Products of lithospheric delamination beneath the Lhasa-Qiangtang collision zone. *Lithos*, *198-199*, 24–37. https://doi.org/10.1016/j.lithos.2014.03.019

Wang, X. C., Xia, B., Liu, W. L., Zhong, Y., Hu, X. C., Guan, Y., et al. (2018). Geochronology, geochemistry and petrogenesis of the Pungco ophiolite, Tibet (in Chinese with English abstract). *Geotectonica et Metallogenia*, *42*(03), 550–569. https://doi.org/10.16539/j.ddgzyckx.2018.03.010

Whalen, J. B., Currie, K. L., & Chappell, B. W. (1987). A-type granites: Geochemical characteristics, discrimination and petrogenesis. *Contributions to Mineralogy and Petrology*, *95*(4), 407–419. https://doi.org/10.1007/bf00402202

Wu, H., Qiangba, Z., Li, C., Wang, Q., Gesang, W., Ciren, O., & Basang, D. (2018). Geochronology and geochemistry of Early Cretaceous granitic rocks in the Dongqiao Area, central Tibet. *Implications for magmatic origin and geological evolution*, *126*(2), 249–260. https://doi.org/10.1086/695702

Wu, H., Sun, S., Liu, H., Chu, H., & Ding, W. (2019). An Early Cretaceous slab window beneath central Tibet, SW China: Evidence from OIB-like alkaline gabbros in the Duolong area. *Terra Nova*, *31*(1), 67–75, d. https://doi.org/10.1111/ter.12370

Wu, J. T.-J., & Wu, J. (2019). Izanagi-Pacific ridge subduction revealed by a 56 to 46 Ma magmatic gap along the northeast Asian margin. *Geology*. https://doi.org/10.1130/g46778.1

Xu, W., Li, C., Wang, M., Fan, J.-J., Wu, H., & Li, X. (2017). Subduction of a spreading ridge within the Bangong Co–Nujiang Tethys Ocean: Evidence from Early Cretaceous mafic dykes in the Duolong porphyry Cu–Au deposit, western Tibet. *Gondwana Research*, *41*, 128–141. https://doi.org/10.1016/j.gr.2015.09.010

Yan, H. Y., Long, X., Wang, X.-C., Li, J., Wang, Q., Yuan, C., & Sun, M. (2016). Middle Jurassic MORB-type gabbro, high-Mg diorite, calc-alkaline diorite and granodiorite in the Ando area, central Tibet: Evidence for a slab roll-back of the Bangong-Nujiang Ocean. *Lithos*, *264*, 315–328. https://doi.org/10.1016/j.lithos.2016.09.002

Yang, Q., Xia, X., Zhang, W., Zhang, Y., Xiong, B., Xu, Y., et al. (2018). An evaluation of precision and accuracy of SIMS oxygen isotope analysis. *Solid Earth Sciences*, *3*(3), 81–86. https://doi.org/10.1016/j.sesci.2018.05.001

Yin, A., & Harrison, T. M. (2000). Geologic evolution of the Himalayan-Tibetan orogen. *Annual Review of Earth and Planetary Sciences*, *28*, 211–280. https://doi.org/10.1146/annurev.earth.28.1.211

Zeng, M., Zhang, X., Cao, H., Ettensohn, F. R., Cheng, W., & Lang, X. (2016). Late Triassic initial subduction of the Bangong-Nujiang Ocean beneath Qiangtang revealed: Stratigraphic and geochronological evidence from Gaize, Tibet. *Basin Research*, *28*(1), 147–157. https://doi.org/10.1111/bre.12105

Zeng, Y.-C., Chen, J.-L., Xu, J.-F., Wang, B.-D., & Huang, F. (2016). Sediment melting during subduction initiation: Geochronological and geochemical evidence from the Darutso high-Mg andesites within ophiolite melange, central Tibet. *Geochemistry, Geophysics, Geosystems*, *17*(12), 4859–4877. https://doi.org/10.1002/2016GC006456

Zhang, L.-L., Zhu, D.-C., Wang, Q., Zhao, Z.-D., Liu, D., & Xie, J.-C. (2019). Late Cretaceous volcanic rocks in the Sangri area, southern Lhasa Terrane, Tibet: Evidence for oceanic ridge subduction. *Lithos*, *326-327*, 144–157. https://doi.org/10.1016/j.lithos.2018.12.023

Zhang, X.-Z., Wang, Q., Dong, Y.-S., Zhang, C., Li, Q.-Y., Xia, X.-P., & Xu, W. (2017). High-pressure granulite facies overprinting during the exhumation of eclogites in the Bangong-Nujiang Suture Zone, central Tibet: Link to flat-slab subduction. *Tectonics*, *36*(12), 2918–2935. https://doi.org/10.1002/2017TC004774

Zhang, Z., Dong, X., Liu, F., Lin, Y., Yan, R., He, Z., & Santosh, M. (2012). The making of Gondwana: Discovery of 650 Ma HP granulites from the North Lhasa, Tibet. *Precambrian Research*, *212-213*, 107–116. https://doi.org/10.1016/j.precamres.2012.04.018

Zhong, Y., Hu, X.-C., Liu, W.-L., Xia, B., Zhang, X., Huang, W., et al. (2017). Age and nature of the Jurassic–Early Cretaceous mafic and ultramafic rocks from the Yilashan area, Bangong–Nujiang suture zone, central Tibet: Implications for petrogenesis and tectonic evolution. *International Geology Review*, 1–23. https://doi.org/10.1080/00206814.2017.1385033

Zhong, Y., Liu, W.-L., Xia, B., Liu, J.-N., Guan, Y., Yin, Z.-X., & Huang, Q.-T. (2017). Geochemistry and geochronology of the Mesozoic Lanong ophiolitic mélange, northern Tibet: Implications for petrogenesis and tectonic evolution. *Lithos*. https://doi.org/10.1016/j.lithos.2017.09.003

Zhu, D.-C., Li, S.-M., Cawood, P. A., Wang, Q., Zhao, Z.-D., Liu, S.-A., & Wang, L.-Q. (2016). Assembly of the Lhasa and Qiangtang terranes in central Tibet by divergent double subduction. *Lithos*, *245*(Supplement C), 7–17. https://doi.org/10.1016/j.lithos.2015.06.023

Zhu, D.-C., Wang, Q., Chung, S.-L., Cawood, P. A., & Zhao, Z.-D. (2019). Gangdese magmatism in southern Tibet and India–Asia convergence since 120 Ma. *Geological Society, London, Special Publications*, *483*(1), 583–604. https://doi.org/10.1144/sp483.14

Zhu, D. C., Wang, Q., Zhao, Z. D., Chung, S. L., Cawood, P. A., Niu, Y. L., et al. (2015). Magmatic record of India-Asia collision. *Scientific Reports*, *5*, 14 289. https://doi.org/10.1038/srep14289

Zhu, D. C., Zhao, Z. D., Niu, Y., Dilek, Y., & Mo, X. X. (2011). Lhasa terrane in southern Tibet came from Australia. *Geology*, *39*(8), 727–730. https://doi.org/10.1130/g31895.1

Zhu, D. C., Zhao, Z. D., Niu, Y. L., Dilek, Y., Hou, Z. Q., & Mo, X. X. (2013). The origin and pre-Cenozoic evolution of the Tibetan Plateau. *Gondwana Research*, *23*(4), 1429–1454. https://doi.org/10.1016/j.gr.2012.02.002